

A Variational Framework for Residual-Based Adaptivity in Neural PDE Solvers and Operator Learning

Juan Diego Toscano^{a,1}, Daniel T. Chen^{a,1}, Vivek Oommen^b,
Jérôme Darbon^a, George Em Karniadakis^{a,2}

^a*Division of Applied Mathematics, Brown University, Providence, 02912, RI, USA*

^b*School of Engineering, Brown University, Providence, 02912, RI, USA*

Abstract

Residual-based adaptive strategies are widely used in scientific machine learning but remain largely heuristic. We introduce a unifying variational framework that formalizes these methods by integrating convex transformations of the residual. Different transformations correspond to distinct objective functionals: exponential weights target the minimization of uniform error, while linear weights recover the minimization of quadratic error. Within this perspective, adaptive weighting is equivalent to selecting sampling distributions that optimize the primal objective, thereby linking discretization choices directly to error metrics. This principled approach yields three benefits: (1) it enables systematic design of adaptive schemes across norms, (2) reduces discretization error through variance reduction of the loss estimator, and (3) enhances learning dynamics by improving the gradient signal-to-noise ratio. Extending the framework to operator learning, we demonstrate substantial performance gains across optimizers and architectures. Our results provide a theoretical justification of residual-based adaptivity and establish a foundation for principled discretization and training strategies.

Keywords: physics-informed learning, PINNs, neural operators, adaptive sampling, PDEs

1. Introduction

Scientific machine learning (SciML) has emerged as a powerful alternative to traditional numerical methods for solving partial differential equations (PDEs). Here, we consider two of the main approaches in SciML. The first, which includes Physics-Informed Neural Networks (PINNs) [1] and their variants [2], focuses on function approximation, where a representation model is trained to satisfy the governing equations of a specific problem [3]. The second is operator learning [4, 5], where a model learns the underlying solution operator itself, allowing it to generate solutions for new boundary conditions, source terms, or parameters almost instantaneously.

At their core, SciML models employ parameterized functions with strong approximation capabilities [6, 7, 8, 9, 10, 11, 12, 13] to represent the solution of a PDE. The problem is thus transformed into an optimization task to find the optimal parameters for this representation.

¹These authors contributed equally to this work

²Corresponding author: george.karniadakis@brown.edu

For physics-informed methods, this typically involves minimizing a loss function composed of the PDE residuals and the mismatch with observational data. This optimization-centric approach provides significant flexibility over traditional methods. For instance, PINN-style methods can easily incorporate sparse data and are not constrained by prescribed boundary conditions, which makes them highly effective for solving inverse problems. Furthermore, they can be scaled to high-dimensional problems, offering a way to mitigate the so-called curse of dimensionality [14]. However, the optimization problems inherent to SciML are generally high-dimensional and non-convex, making models susceptible to converging to poor local minima. Consequently, tackling the optimization has drawn significant research attention, with efforts including the development of specialized optimizers [15, 16, 17] and methods that simplify the optimization task by explicitly encoding physical constraints, such as the exact imposition of boundary conditions [18, 19].

Among the various approaches, one of the most prominent strategies, which addresses both optimization and discretization errors, is to modify the loss function itself. This is typically achieved through adaptive sampling [20, 21] and weighting schemes [22, 23, 24, 25, 26, 27]. Instead of altering the model or the PDE, these techniques dynamically adjust the training process to focus on regions of the domain that are more difficult to learn. Adaptive sampling methods achieve this by concentrating collocation points in areas where the PDE residual is high [21, 28, 29], while adaptive weighting methods assign larger local weights to these same important regions. The strategies for determining these weights are diverse, ranging from direct residual-based schemes to more complex adversarial or augmented Lagrangian formulations [23, 22, 26, 30].

Due to their simplicity and efficiency, methods based on the residuals are particularly popular, as they do not require specialized architectures or additional parameters. Two such examples are residual-based attention (RBA), which applies adaptive weights, and the residual-based adaptive distribution (RAD), which modifies the sampling of collocation points [31, 32, 33, 34, 35, 36, 37, 38, 39, 40]. Although these methods intuitively aim for the same goal of directing the optimizer’s attention to high-error regions, no direct link between them has been established. Furthermore, while focusing on high-error regions seems beneficial, a formal argument for its efficiency has been lacking. These heuristic strategies are conceptually related to importance sampling; however, there is a critical difference. Standard importance sampling reweights the sample to produce an unbiased estimator with less variance, whereas the schemes used in SciML estimate the desired functionals under an adaptively biased distribution. To the best of our knowledge, no theoretical understanding of this adaptive biasing in SciML exists.

In this work, we address this gap by proposing a general framework for deriving these sampling and weighting schemes. The formulation is most clearly seen by changing the objective function from the usual mean-squared error (L^2) to the maximum error (L^∞) over the spatial domain. Leveraging variational formulas, we show that minimizing the L^∞ -norm can be written in a dual form that naturally involves sampling adaptively from distributions exponentially tilted by the current residual. These new distributions can be realized through either direct sampling or importance weights, thereby providing a formal justification and unification for these training schemes. More general loss functions, such as the L^2 norm, can be recovered from this dual formulation using variational representations of more general statistical divergences. We refer to the multipliers obtained from this variational approach

as variational residual-based attention (vRBA).

Our unified framework provides a principled origin for heuristics like RBA and RAD, showing how different potential functions correspond to different adaptive schemes. We extend these methods to operator learning with a hybrid strategy employing importance sampling over the function space and importance weighting over the spatial domain, which can be seamlessly integrated into architectures like FNO and DeepONet. The framework yields a twofold benefit: it lowers the discretization error by reducing the variance of the loss estimator, and it improves learning dynamics by enhancing the signal-to-noise ratio of the gradients, leading to faster convergence. Finally, we demonstrate the efficacy of vRBA across a range of challenging PINN and operator learning tasks. Our empirical results show that using vRBA is critical to achieve lower errors, providing significant improvements even when paired with state-of-the-art second-order optimizers [16] or specialized architectures like TC-UNet [41].

2. Problem Setup

For a domain $\Omega \subset \mathbb{R}^d$, define the residual $r : \Omega \rightarrow \mathbb{R}_+$ to be a bounded function describing the error at each spatial point $x \in \Omega$. For example, in supervised learning tasks such as function approximation, one seeks to approximate some function $\bar{u} : \Omega \rightarrow \mathbb{R}$ with a parameterized $u(x; \theta)$, for parameters θ in some parameter space \mathcal{T} . Then, the residual is defined as follows

$$r(x) := |\bar{u}(x) - u(x; \theta)|. \quad (1)$$

On the other hand, PINNs, the residual is given by an appropriate differential operator \mathcal{F} applied onto the parameterized function which reads

$$r(x) := |\mathcal{F}[u(\cdot; \theta)]|. \quad (2)$$

In either case, one would like to find the parameter θ^* that minimizes the residual, to approximate the unknown function \hat{u} or to solve the differential equation $\mathcal{F}[u] = 0$, by defining a loss function \mathcal{L} in terms of the residuals and solving for

$$\theta^* = \arg \min_{\theta \in \mathcal{T}} \mathcal{L}(\theta, \Omega).$$

There are many possible choices of loss functions. In the ideal scenario, one would like to find the parameter that minimizes the residual *uniformly* over all points in the spatial domain, i.e., we seek the solution to the following optimization problem

$$\min_{\theta} \left\{ \max_{x \in \Omega} r(x, \theta) \right\}. \quad (\text{P1})$$

In other words, we wish to minimize the $L^\infty(\Omega)$ -norm of the residual. Alternatively, we can (superfluously) write (P1) as an optimization over the space of probability measures

$$\min_{\theta} \left\{ \max_{q \in \mathcal{P}(\Omega)} \int_{\Omega} r(x, \theta) q(dx) \right\} \quad (3)$$

where the optimizer of the inner maximum is $q^* = \delta_{x^*}$ and $x^* = \arg \max_{\Omega} r$.

(P1) is rarely used in practice due to its instability and non-differentiability. Moreover, the optimization landscape induced by the parameterization is extremely non-convex and identically-zero residual is impossible for most parameterization schemes, e.g., neural networks, despite the availability of asymptotic approximation theorems [42, 43, 44]. Consequently, the popular alternative is to solve a “weaker” problem by solving

$$\min_{\theta} \left\{ \int_{\Omega} r(x, \theta)^2 p(x) dx \right\} \quad \text{where } p(x) = \frac{\mathbf{1}_{x \in \Omega}}{|\Omega|} \quad (\text{P2})$$

and $|\Omega|$ refers to the volume of the domain. This corresponds to the $L^2(\Omega)$ norm of the residuals and (P1) is stronger than (P2) in the sense that any near-optimizers of (P1) are also near-optimizers in (P2).

Remark 2.1. In the context of PINNs, one’s goal is to find the solution to certain partial differential equation. Then, solutions where (P1) are zero correspond to classical solutions of differential equations, i.e., k -times continuously-differentiable functions $u \in \mathcal{C}^k(\Omega)$ for some $k \geq 1$ corresponding to the highest-order derivatives in the respective differential operator. Under this interpretation, one can potentially argue that (P1) is a more natural optimization problem to consider than (P2).

Under (P2), we define the loss function

$$\mathcal{L}(\theta) = \int_{\Omega} r(x, \theta)^2 p(x) dx, \quad (4)$$

which can be easily approximated via Monte Carlo integration, that is, let $(X_i)_{i=1}^N$ be independent samples from p , and define the discrete loss

$$\mathcal{L}^{(D)}(\theta) = \frac{1}{N} \sum_{i=1}^N r^2(X_i, \theta). \quad (5)$$

The discrete domain $D = (X_i)_{i=1}^N$ is also called the quadrature or the collocation points. Minimizing this discrete loss is equivalent to minimizing the empirical mean-squared error (MSE) of a set of points randomly selected from the domain of interest.

2.1. Reformulating loss function for adaptive training

The discrete loss formulation (e.g., Equation (5)) has been observed to cause difficulties for certain problems. For instance, in PINNs for solving complex PDEs (e.g., Allen-Cahn or Burgers’ equations), it can lead to slow convergence or convergence to an incorrect solution [1]. In response, two primary families of approaches have been proposed to modify the loss computation at each step of the training process.

One family of methods involves sampling the quadrature points according to a suitable residual-based distribution [20, 21, 28, 29, 45, 46, 47, 48, 49, 50, 51, 52, 53]. A widely adopted example is the residual-based adaptive distribution (RAD) [21], where instead of sampling

the quadrature points from the base distribution p , one would sample from an adaptive, tilted distribution computed as follows

$$q_{\text{RAD}}^k(x) \propto \frac{r(x)^\nu}{\mathbb{E}_p[r(x)^\nu]} + c \quad (6)$$

where ν and c are hyperparameters and k is the index of the current iteration.

A second line of work, with seminal contributions from [22], proposes modifying Equation 5 by assigning local multipliers λ_i to each collocation point X_i and computing a weighted sum instead. More explicitly, one can compute an alternative loss function of the form

$$\mathcal{L}_W^{(D)}(\theta) = \frac{1}{N} \sum_{i=1}^N [\lambda_i r(X_i, \theta)]^2,$$

while numerous proposals have been made for the specific form of λ_i [22, 54, 26, 55, 25, 23, 56, 57, 58, 36]. One of the most effective methods define the multipliers explicitly from the residual, as in the residual-based-attention (RBA) method: for the spatial point X_i , we set

$$\lambda_i^k \propto \frac{r(X_i)}{\sum_j r(X_j)}. \quad (7)$$

In practice, for stability, the local multipliers computation often involves an exponential moving average of the form $\lambda_i^k = \gamma \lambda_i^{k-1} + \frac{\eta}{\max_{\Omega} q} q_i^k$.

Both approaches, therefore, follow a general theme: they modify the objective in Equation 5 to bias the optimization towards high-error regions. These methods have been widely adopted and have proven quite successful; however, their theoretical foundation remains elusive.

2.2. Learning Dynamics

Once the objective function (\mathcal{L}) is calculated, the model parameters are generally optimized using a line search algorithm of the form

$$\theta^{k+1} = \theta^k + \alpha^k p^k \quad (8)$$

where α^k is the step size, and $p^k = -H_k \nabla_{\theta} \mathcal{L}(\theta^k)$ is the update direction which depends on the gradient of the objective function and some symmetric matrix H_k [16]. For first-order optimizers such as Adam [59], H_k is treated as the identity matrix. Therefore, for the discrete case, the update direction induced by Equation (5) is given by

$$\hat{p}_k := -\nabla_{\theta} L^{(D)}(\theta) = -\frac{1}{N} \sum_{i=1}^N \nabla_{\theta} r(X_i, \theta^k)^2. \quad (9)$$

Notice that a successful optimization would be achieved if the discrete update direction contains enough information to minimize the loss in the whole domain. However, even if the sampling is performed only once at the beginning of training and the full data is used to perform the update stage (commonly referred to as full-batch training), the optimization process can lead to imbalances.

Lemma 2.2. For a discrete domain D of size $N = Mb$, define $\{B_j\}_{j=1}^b$ to be an equal-sized partition of D , that is

$$\bigcup_{j=1}^b B_j = D, \quad B_j \cap B_{j'} = \emptyset \quad \text{for } j \neq j', \quad \text{and } |B_j| = M \quad \text{for all } j = 1, \dots, b.$$

Letting $\hat{p}_j^k = -\nabla_{\theta} \mathcal{L}^{(B_j)}(\theta^k)$ be the update direction using the batch B_j , the full-batch update direction is the average of the update directions of its partitions

$$\hat{p}^k = \frac{1}{b} \sum_{j=1}^b \hat{p}_j^k$$

Proof. The proof follows from the linearity of the gradient operator. The loss on the full discrete domain, Equation (5), can be expressed as the average of the losses on the partitions $\{B_j\}$.

$$\begin{aligned} \mathcal{L}^{(D)}(\theta) &= \frac{1}{N} \sum_{i=1}^N r^2(X_i, \theta^k) = \frac{1}{bM} \sum_{j=1}^b \sum_{x \in B_j} r^2(x, \theta) \\ &= \frac{1}{b} \sum_{j=1}^b \left(\frac{1}{M} \sum_{x \in B_j} r^2(x, \theta) \right) \\ &= \frac{1}{b} \sum_{j=1}^b \mathcal{L}^{(B_j)}(\theta) \end{aligned}$$

Applying the negative gradient operator $-\nabla_{\theta}$ to both sides yields the result. \square

The arbitrary partitioning of the dataset highlights a critical challenge. Even when considering the full dataset (i.e., a single computation or full batch), the gradients implicitly computed from different data partitions may point in conflicting directions. If these component gradients are not in alignment, their average, which constitutes the full-batch gradient, can be diminished or misleading, leading to slow convergence or stagnation.

2.3. Signal-to-Noise Ratio (SNR)

As shown in the preceding section, gradient disagreement is not merely an artifact of stochastic sampling; it is an inherent property of the loss landscape, observable even within a single, complete batch of data. To analyze these variations, several studies [60, 61, 62] have considered the signal-to-noise ratio (SNR). A common formulation for the SNR of a gradient vector reads

$$\text{SNR} = \frac{\|\mathbb{E}_{B_j}[\hat{p}_j^k]\|_2}{\sqrt{\text{Tr}(\text{Var}_{B_j}[\hat{p}_j^k])}} \quad (10)$$

where the expectation \mathbb{E}_{B_j} and variance Var_{B_j} are taken over the random selection of a partition B_j from the full dataset.

To formalize this, we can decompose the update direction \hat{p}_j^k from a partition B_j relative to the true update direction from the continuous loss in Equation (4), which we define as our “signal”: $\hat{p}^k = -\nabla_{\theta}\mathcal{L}^{(D)}(\theta^k)$. The partition-based direction is

$$\hat{p}_j^k = \hat{p}^k + \epsilon_i^k,$$

where ϵ_i^k is the deviation induced by the discretization and the specific choice of partition B_j . The discrete partition gradients are unbiased in the sense that $\mathbb{E}_{B_j}[\hat{p}_j^k] = \hat{p}^k$, it follows that the noise term has zero mean:

$$\mathbb{E}_{B_j}[\epsilon_i^k] = \mathbb{E}_{B_j}[\hat{p}_j^k - \hat{p}^k] = \mathbb{E}_{B_j}[\hat{p}_j^k] - \hat{p}^k = 0.$$

On the other hand, \hat{p}_j^k has covariance

$$\begin{aligned} \text{Var}_{B_j}[\hat{p}_j^k] &= \mathbb{E}_{B_j} [(\hat{p}_j^k - \mathbb{E}_{B_j}[\hat{p}_j^k])(\hat{p}_j^k - \mathbb{E}_{B_j}[\hat{p}_j^k])^T] \\ &= \mathbb{E}_{B_j} [(\hat{p}^k + \epsilon_i^k - \hat{p}^k)(\hat{p}^k + \epsilon_i^k - \hat{p}^k)^T] \\ &= \mathbb{E}_{B_j}[\epsilon_i^k(\epsilon_i^k)^T]. \end{aligned}$$

The denominator in the SNR formula corresponds to the noise power, which is the trace of this covariance matrix

$$\text{Tr}(\text{Var}_{B_j}[\hat{p}_j^k]) = \mathbb{E}_{B_j}[\text{Tr}(\epsilon_i^k(\epsilon_i^k)^T)] = \mathbb{E}_{B_j}[\|\epsilon_i^k\|_2^2].$$

Therefore, the SNR is given by the ratio of the magnitude of the signal (the true update direction) to the root mean square (RMS) magnitude of the noise (the deviations due to partitioning). This phenomenon of quantifying the disagreement, or “noise”, between gradients has been analyzed extensively in the context of stochastic and minibatch training [60]. Similar metrics have also been studied for different problem settings, such as multiobjective loss functions [63].

2.4. Stages of Learning

The SNR provides insight into the deterministic and stochastic regimes of the training process, where high SNR corresponds to confident, deterministic updates, and low SNR indicates a more exploratory, stochastic phase [64]. By tracking the evolution of the SNR, recent studies have identified three distinct stages of learning: fitting, transition, and diffusion. This phased progression has been observed across a variety of domains, including function approximation [64, 9], PINNs [61, 57], and operator learning [9], for diverse representation models such as MLPs and KANs. The three stages can be described as follows:

Fitting. This is the initial phase of training. The process begins with large gradients and high agreement between subdomain updates, yielding a high SNR. During this deterministic phase, the model rapidly reduces the training error by learning the dominant trends in the data. As these general features are captured, however, disagreements between subdomains on finer details emerge, causing the SNR to decrease. This stage is thus characterized by a sharp initial reduction in training error with minimal improvement in generalization error, accompanied by an increase in the model’s geometric complexity [64].

Transition. Following the initial fit, the model enters an exploratory stage characterized by a sustained low SNR. Here, the model attempts to reconcile conflicting objectives from different subdomains, but there is no consensus on an optimal update direction. Consequently, this phase exhibits little to no improvement in the generalization error, while the geometric complexity may continue to increase as the model explores the solution space [61, 57].

Diffusion. After a period of exploration, the model may become sufficiently complex to find a parameter configuration that realigns the subdomain gradients. This leads to a sudden increase in the SNR, marking the beginning of the productive diffusion phase. Once this consensus direction is found, the generalization error improves significantly. Concurrently, the geometric complexity often decreases as the model identifies an efficient internal representation. Eventually, as the loss converges and the gradient magnitudes (the signal) diminish, the SNR naturally decays again, at which point learning slows down and the generalization error plateaus.

One of the main advantages of this approach is that it provides a measure of convergence that can be used to evaluate a model’s performance. Previous studies [61, 57] have shown that the best-performing models typically reach the total diffusion phase earlier than others; moreover, in general, they maintain a consistently higher SNR. Conversely, models that fail to converge, often remain trapped in the diffusion stage, unable to progress further [3].

3. A framework for approximate uniform minimization

In this work, we propose a dual formulation of (P1) inspired by the following problem

$$\min_{\theta \in \mathcal{T}} \max_{q \in \mathcal{P}(\Omega)} \left\{ \int_{\Omega} r(x; \theta) q(dx) + \epsilon \mathbf{H}(q|p) \right\} \quad \text{for } 0 < \epsilon \ll 1$$

where \mathbf{H} denotes the relative entropy or the Kullback-Leibler divergence (cf. (11)). See (P1*) for the exact dual problem. Note the similarity between the above variational problem and (3): the two problems are equivalent when the regularizer ϵ is zero. However, for non-zero ϵ , we enforce absolute continuity of the *test measure* q with the *base measure* p and exclude singular choices of q , such as the optimizer of (3). The dual formulation enables stability of training throughout while adaptively improving parts of the domains with higher residuals.

3.1. A dual reformulation

To arrive at the dual form of (P1), we use the Laplace principle (Appendix A.1), which writes the maximum as a limit of integrating an increasing singular exponential functional

$$(\text{P1}) = \min_{\theta \in \mathcal{T}} \sup_{\epsilon > 0} \left\{ \epsilon \log \int_{\Omega} e^{r(x; \theta)/\epsilon} p(dx) \right\} \geq \sup_{\epsilon > 0} \min_{\theta \in \mathcal{T}} \left\{ \epsilon \log \int_{\Omega} e^{r(x; \theta)/\epsilon} p(dx) \right\}.$$

To arrive at the desired form, we further express the inner functional using the Gibbs variational formula (Appendix A.2)

$$\max_{\epsilon > 0} \min_{\theta \in \mathcal{T}} \max_{q \in \mathcal{P}(\Omega)} \left\{ \int_{\Omega} r(x; \theta) q(dx) - \epsilon \mathbf{H}(q|p) \right\} \quad (\text{P1}^*)$$

where \mathbf{H} is the relative entropy

$$\mathbf{H}(q|p) = \begin{cases} \int_{\Omega} \log \frac{dq}{dp}(x)q(dx) & \text{if the Radon-Nikodym derivative } \frac{dq}{dp} \text{ exists,} \\ +\infty & \text{otherwise.} \end{cases} \quad (11)$$

The innermost optimization admits a closed-form solution (see [Appendix A.2](#)) which reads

$$q^*(dx) = \frac{e^{r(x;\theta)}}{\int_{\Omega} e^{r(x';\theta)}p(dx')}p(dx) = \arg \max_{q \in \mathcal{P}(\Omega)} \left\{ \int_{\Omega} r(x;\theta)q(dx) - \epsilon \mathbf{H}(q|p) \right\}.$$

Remark 3.1. The Laplace principle, referred to also as Varadhan’s lemma [65, Theorem 4.3.1], has a long history in the area of statistical physics and large deviations theory. In combination with a theorem from Bryc and the Gibbs variational principle, the Laplace principle gives an alternative characterization for large deviations principles and is foundational for the development of the *weak convergence approach* to large deviations of Dupuis and Ellis [66, 67]; the computation used to derive the dual form is reminiscent of the techniques used in this weak convergence approach. Similar exponential functionals are known in the community as the softmax function, commonly used in machine learning, Bayesian statistics, and transformers as a smooth approximation of the maximum function. A similar family of probability distributions was recently used by Alberts and Bilonis [68] for uncertainty quantification. The inverse temperature β plays the role of $1/\epsilon$ in this manuscript.

The formulation of (P1*) gives rise to a natural alternating optimization scheme. At each iteration, we solve the innermost optimization to the outermost. Fix initial conditions $q^0, \theta^0, \epsilon^0$, define the iterations for the $k + 1$ -th iteration given the k -th:

$$\left\{ \begin{array}{l} q^{k+1}(dx) \leftarrow \frac{1}{Z^k} \exp\left(\frac{r(x;\theta^k)}{\epsilon^k}\right) p(dx) \text{ where } Z^k = \int_{\Omega} \exp\left(\frac{r(x;\theta^k)}{\epsilon^k}\right) p(dx); \\ \theta^{k+1} \leftarrow \text{Minimize } \int_{\Omega} r(x, \theta^k) q^{k+1}(dx); \\ \epsilon^{k+1} \leftarrow \text{AnnealingScheme}(k, \epsilon^k, \theta^{k+1}, q^{k+1}). \end{array} \right. \quad (12)$$

There are two design choices. The oracle `Minimize` refers to equation (8) such as gradient descent and various higher-order methods. On the other hand, `AnnealingScheme` refers to a schedule that incrementally decreases ϵ . For every fixed θ and q , the objective function in (P1*) is maximized by taking $\epsilon \rightarrow 0$ ([Appendix A.1](#)). However, since the optimization in θ takes place incrementally, the outer-loop optimization ought to take place in accordance with the inner loop. For example, an annealing scheme used in numerical experiments is of the form

$$\text{AnnealingScheme}(k, \epsilon, \theta, q) = \frac{c \max_{\Omega} u(\cdot; \theta)}{\log 2 + k},$$

which approaches zero as $k \rightarrow \infty$.

We contrast the proposed algorithm with simulated annealing [69, 70, 71]—which was the source of the terminological choice and the annealing schedule [71, Theorem 1]—where

given a sufficiently smooth potential $V : \Theta \rightarrow \mathbb{R}$, one finds the solution to $\min_{\Theta} V$ to be the long-time behavior ($t \rightarrow \infty$) of the solution to the stochastic differential equation

$$d\theta_t = -\nabla V(\theta_t)dt + \sqrt{2\epsilon_t}dB_t$$

where B is a standard Brownian motion and ϵ_t is an annealing scheme (that is, $\epsilon^k \rightarrow 0$ as $k \rightarrow \infty$). On the other hand, a formal functional central limit theorem suggests that the parameters obey the stochastic equation

$$d\theta_t = -\mathbb{E}_{q_t} [\nabla_{\theta} r(\cdot; \theta)] dt + \sqrt{\text{Var}_{q_t} [\nabla_{\theta} r(\cdot; \theta)]} dB_t$$

where q_t depends on ϵ_t through

$$q_t(dx) \propto e^{r(x; \theta_t)/\epsilon_t} p(dx).$$

First, we remark that the “potential” in this case varies with ϵ_t . Also, unless $r(\cdot; \theta)$ has a unique maximum for all θ , the limit of q_t is non-degenerate and the variance does not vanish, which marks a second difference. For these reasons, we simply draw formal connections between vRBA and simulated annealing but do not claim rigorous equivalences.

3.2. Generalization of dual formulation

Recall that Laplace’s principle rewrites the L^{∞} -norm by exponentially weighting spatial domains with large residuals which dominate the integral. One can argue that similar concentration phenomena should hold for pairings besides the canonical log-exp one. In this subsection, we pursue this generalization to obtain a variational representation for RBA of the same form. Our strategy is an inverse one: we start with a representation formula of form (P1*) and attempt to reverse-engineer the primal minimization objective.

Consider *potential function* $\Phi : \mathbb{R}_+ \rightarrow \mathbb{R}_+$ to be convex, bounded from below, and superlinear, that is,

$$\lim_{r \rightarrow \infty} \frac{\Phi(r)}{r} = +\infty.$$

The starting point of the generalization is to replace the relative entropy with the more general Φ -divergence, defined by

$$\mathbf{D}_{\Phi}(q|p) := \begin{cases} \int_{\Omega} \Phi \left(\frac{dq}{dp}(x) \right) p(dx) & \text{if the Radon-Nikodym derivative } \frac{dq}{dp} \text{ exists,} \\ +\infty & \text{otherwise.} \end{cases}$$

For strictly convex, superlinear Φ , the statistical divergence is also convex, lower semicontinuous, and zero if and only if $q = p$.

We propose the generalized dual optimization problem:

$$\sup_{\epsilon > 0} \min_{\theta \in \mathcal{T}} \sup_{q \in \mathcal{P}(\Omega)} \{ \mathbb{E}_q [r(x; \theta)] - \epsilon \mathbf{D}_{\Phi^*}(q|p) \} \quad (13)$$

where Φ^* is the convex conjugate (or the Legendre-Fenchel transform) of Φ , i.e.,

$$\Phi^*(s) = \sup_{s \in \mathbb{R}} \{sr - \Phi(r)\}.$$

Restricting Φ to convex, suplinear functions guarantees that Φ^* is the same. Similar to relative entropy, the innermost optimization also admits a generalized Gibbs variational representation [72] (see [Appendix A.3](#) for a statement), albeit with a more complicated form:

$$\inf_{\nu \in \mathbb{R}} \{\nu + \mathbb{E}_p[\Phi(r - \nu)]\} = \sup_{q \in \mathcal{P}(\Omega)} \{\mathbb{E}_q[r(x; \theta)] - \epsilon \mathbf{D}_{\Phi^*}(q|p)\}$$

From here and following steps in [Section 3.1](#), it follows that [\(13\)](#) is a dual formulation for minimizing the following norm-like quantity:

$$\min_{\theta \in \mathcal{T}} \sup_{\epsilon > 0} \{\Lambda_\epsilon(r)\} \quad \text{where} \quad \Lambda_\epsilon(r) := \inf_{\nu \in \mathbb{R}} \left\{ \epsilon \Phi^{-1} \left(\frac{\nu}{\epsilon} + \int_{\Omega} \Phi \left(\frac{r(x; \theta) - \nu}{\epsilon} \right) p(dx) \right) \right\} \quad (14)$$

where we reparameterized $\nu \mapsto \nu/\epsilon$ and moved the infimum to the outside as Φ^{-1} is monotonic.

In the absence of a specific Φ , the functional $\lim_{\epsilon \rightarrow 0} \Lambda_\epsilon$ is difficult to interpret. We enumerate several special cases that can be of interest.

1. $\Phi(r) = e^r$ recovers the Laplace's principle.
2. $\Phi(r) = r^2 + 1$, the corresponding Φ^* -divergence is the chi-squared divergence and the objective function in the primal problem is the standard deviation (cf. [Appendix A.4](#)):

$$\lim_{\epsilon \rightarrow 0} \Lambda_\epsilon(r) = \sqrt{\mathbb{E}_p[r^2] - \mathbb{E}_p[r]^2}. \quad (15)$$

Note that this primal problem is not well-posed: in the context of PINNs, the solutions learned are the ones of the form $\mathcal{F}[u] = c$ for any $c \in \mathbb{R}$. However, by choosing the annealing scheme ϵ^k a particular way, one could obtain a dual formulation that is well-posed and corresponds to the $L^2(\Omega)$ -norm (see discussion below).

3. Taking $\nu = 0$, when the inequality

$$p\Phi(r) \leq r\Phi'(r) \leq q\Phi(r)$$

is satisfied for some $p, q \in (1, \infty)$ —which includes the case where $\Phi(r) = r^p$ —then by [\[73, Equation 3\]](#), we have

$$\frac{1}{c} \|r\|_{L^p(\Omega)} \leq \Lambda_\epsilon(r) \leq c \|r\|_{L^q(\Omega)} \quad \text{for } c = \left(\frac{p}{q}\right)^{1/p}.$$

A crucial step component is lost in this generalization: the generalized Gibbs variational formula lacks a general form of the optimizer in the innermost optimization of [\(13\)](#). In particular, we only know that q is optimal when

$$q(dx) = \Phi' \left(\frac{r(x; \theta)}{\epsilon} \right) p(dx),$$

which can only hold under an additional normalization condition

$$\int_{\Omega} \Phi' \left(\frac{r(x; \theta)}{\epsilon} \right) p(dx) = 1, \quad (16)$$

and is not always achieved. Hence, we rely on the choice of the annealing scheme to ensure (16) is always satisfied. For example, if $\Phi(r) = r^2 + 1$, $\Phi'(r) = 2r$ and ϵ^k can be chosen directly to be whatever constant normalizes the kernel

$$q^k(dx) = \frac{r(x; \theta^k)}{\int_{\Omega} r(x; \theta^k) p(dx)} p(dx).$$

Satisfying (16) implies that the optimal ν in (14) is achieved at zero (Item 2 of [Appendix A.3](#)), which recovers the canonical choice of minimizing the $L^2(\Omega)$ -norm.

Remark 3.2. The functional Λ_{ϵ} has connections to the *Jensen sums*, which are studied in convex analysis and have relations with *Orlicz spaces* L^{Φ} . For convex, superlinear potentials Φ , Orlicz spaces are Banach spaces equipped with the Luxembourg norm

$$\|f\|_{\Phi} = \inf \left\{ \epsilon > 0 : \int_{\Omega} \Phi(|f(x)|/\epsilon) p(dx) \leq 1 \right\}.$$

Due to the similarity of forms, we conjecture connections between the asymptotics of the functional $\lim_{\epsilon \rightarrow 0} \Lambda_{\epsilon}$ to Orlicz spaces. However, to limit the scope of the paper, we defer a detailed theoretical and numerical investigation of general choices of Φ —as well as implications to optimization and interpretations in the context of PINNs and related machine learning tasks—to future work.

3.3. Discretization

An outstanding issue in implementing (12) is the tractability of integrating against the measure q^k . Even when p is a simple measure, e.g., uniform on a domain Ω or Gaussian, the exponential tilt—particularly the normalizing constant Z^k —is typically expensive to compute as it requires fine discretization of the mesh. Generally, updating q^k only after several iterations suffices to reduce the computational complexity.

However, when p is a distribution easy to sample from, one can approximate the expectation via Monte Carlo and a change-in-measure. That is, let $(X_i)_{i=1}^n$ be independent and identically-distributed (i.i.d.) samples from p . Then, we can approximate $\mathbb{E}_{q^k}[r]$ for any measurable functional $r : \Omega \rightarrow \mathbb{R}$, i.e., the residual or its gradient, by

$$\mathbb{E}_{q^k}[r] = \mathbb{E}_p \left[r \frac{dq^k}{dp} \right] = \lim_{n \rightarrow \infty} \frac{1}{n} \sum_{i=1}^n \frac{dq^k}{dp}(X_i) r(X_i).$$

This is an *unbiased* estimator for the expectation of r over q^k . However, in this context, the Radon-Nikodym derivative has an integral (the normalizing constant) that is difficult to compute. Therefore, we resort to approximating the integral with Monte Carlo samples, e.g.,

$$\mathbb{E}_{q^k}[r] = \lim_{n \rightarrow \infty} \hat{r}^n := \frac{\sum_{i=1}^n e^{r(X_i; \theta^k)/\epsilon^k} r(X_i)}{\sum_{j=1}^n e^{r(X_j; \theta^k)/\epsilon^k}} \quad p/q^k\text{-almost-surely.}$$

In particular, we can define the *multipliers*

$$\lambda_i^k := \frac{e^{r(X_i; \theta^k)}}{\sum_j e^{r(X_j; \theta^k)}} \quad \text{which gives} \quad \hat{r}^n = \sum_{i=1}^n \lambda_i^k r(X_i), \quad (17)$$

and hence we recover the form of the estimator popularly used in the PINNs community. Estimating the normalizing constant introduces bias to the estimator, though the estimator is nonetheless consistent and enjoys the central limit

$$\lim_{n \rightarrow \infty} \sqrt{n} (\hat{r}^n - \mathbb{E}_{q^k}[r]) \rightarrow \mathbf{N} \left(0, \text{Var}_p \left[r \frac{dq^k}{dp} \right] \right) \quad \text{in distribution,}$$

where $\mathbf{N}(\mu, \sigma^2)$ is a Gaussian measure with mean μ and variance σ^2 . In other words, the discretization error vanishes on the order of $\mathcal{O}(1/\sqrt{n})$ with constants that scale with the variance. In the context of RBA, if the following inequality holds:

$$\text{Var}_p \left[r \frac{dq^k}{dp} \right] \leq \text{Var}_p [r],$$

then the discretization error obtained from reweighting is lower than that without; this indeed is observed empirically as demonstrated in the later sections.

As a final remark particularly relevant for operator learning: if the domain is a product space $\Omega = \Omega_1 \times \Omega_2$ equipped with a product measure $p(dx_1, dx_2) = p(dx_1)p(dx_2)$, the Radon-Nikodym derivatives can be disintegrated to facilitate implementation. More specifically, one rewrites

$$\mathbb{E}_{q^k}[r] = \int_{\Omega} \frac{dq^k}{dp}(x) r(x) p(dx) = \int_{\Omega_1} \frac{dq^k}{dp}(x_2) \int_{\Omega_2} \frac{dq^k}{dp}(x_1|x_2) r(x_1, x_2) p(dx_1) p(dx_2) \quad (18)$$

where

$$\frac{dq^k}{dp}(x_1|x_2) = \frac{\frac{dq^k}{dp}(x_1, x_2)}{\int_{\Omega_2} \frac{dq^k}{dp}(x_1, x_2) p(dx_1)} \quad \text{and} \quad \frac{dq^k}{dp}(x_2) = \frac{\int_{\Omega_2} \frac{dq^k}{dp}(x_1, x_2) p(dx_1)}{\int_{\Omega} \frac{dq^k}{dp}(x) p(dx)}.$$

From here, one can choose to sample or weight either coordinate. For example, in operator learning, the domain is a product of some function space and the spatial domain that the functions is defined on. We then compute the vRBA estimate by sampling over function space and computing multipliers for the spatial domain.

4. Methods

4.1. Variational Residual-based Attention Methods

As described in the previous section, the general method is flexible, allowing for the use of different potential functions, Φ , with particular properties.

The training process starts by sampling N i.i.d. random variables $\{X_i\}_{i=1}^N$ uniformly from the domain Ω and calculating the corresponding residuals $r(X_i)$. The general method then involves three steps per iteration: (1) updating the tilted distribution q , (2) updating the model parameters θ via a line search method, and (3) updating the temperature parameter ϵ using an annealing scheme.

4.1.1. Update the tilted distribution

While the generalized Gibbs variational principle does not typically yield a closed-form update rule for the distribution q , one can obtain the optimal tilt by choosing specific potentials Φ and annealing schedules (to be discussed in the coming subsection). Under the appropriate choices, q is proportional to the derivative of the potential Φ' . For a discrete set of points, the optimal probability mass function (p.m.f.) for the next iteration, q^{k+1} , is given by

$$q^{k+1}(X_i) \propto \Phi' \left(\frac{r(x_i; \theta^k)}{\epsilon^k} \right) \quad (19)$$

We consider two particular cases for Φ .

Case I: $\Phi(x) = e^x$. This choice of potential recovers the Laplace principle, which is associated with minimizing the L^∞ norm, and there is an exact convex duality. The derivative is $\Phi'(x) = e^x$, so the optimal distribution is proportional to $\exp(|r|/\epsilon)$ under no additional assumptions. This resulting distribution is given by a variation of the *softmax* of the scaled residuals akin to attention mechanisms popularized in the transformer architecture [74]

$$q^{k+1}(X_i, \theta^k) = \frac{\exp \left(\frac{r(X_i; \theta^k)}{\epsilon^k} \right)}{\sum_{j=1}^N \exp \left(\frac{r(X_j; \theta^k)}{\epsilon^k} \right)} \quad (20)$$

Case II: $\Phi(x) = x^2 + 1$. In this case, the derivative is $\Phi'(x) = 2x$, which is associated with minimizing the L^2 norm. In this case, the convex duality is not exact, and the appropriate annealing schedule will be chosen shortly. The discretized p.m.f. takes the following form

$$q^{k+1}(X_i, \theta^k) = \frac{|r(X_i, \theta^k)|}{\sum_{j=1}^N |r(X_j, \theta^k)|} \quad (21)$$

Finally, since the collocation points $\{X_i\}$ are randomly sampled and the target distribution q^{k+1} depends on the current model parameters, the resulting p.m.f. can be prone to spurious fluctuations. To promote stability, especially when using fast-growing potentials like $\Phi(r) = e^r$ that can create sharply peaked distributions, we smooth the target distribution over time using an exponential moving average (EMA).

Furthermore, we introduce an additional smoothing mechanism by interpolating between the adaptive distribution q^{k+1} and the base uniform distribution p_u . The combined update rule for the importance weights reads

$$\lambda_i^{k+1} = \gamma \lambda_i^k + \eta^* (\phi q^{k+1}(X_i, \theta^k) + (1 - \phi) p_u(X_i))$$

where $\gamma \in [0, 1)$ is a memory term and η^* is a learning rate. The parameter $\phi \in [0, 1]$ controls the degree of adaptivity; $\phi = 1$ corresponds to the fully adaptive case from which the original method is recovered, while smaller values of ϕ increase stability by biasing the distribution towards uniformity. For stability reasons, which becomes particularly important for second-order methods, we have found that normalizing the learning rate as $\eta^* = \eta / \max_{\Omega} q^{k+1}$ is beneficial.

The resulting vector λ^{k+1} can be interpreted as the smoothed, unnormalized distribution that guides the optimization. While it incorporates information from the optimal distribution q^{k+1} , it is not itself a probability mass function (p.m.f.) as it does not necessarily sum to one.

4.1.2. Update the model parameters

Once the smoothed importance weights $\{\lambda_i^{k+1}\}$ have been computed, they can be used to formulate the loss function in two primary ways: by guiding a resampling process or by directly weighting the residuals.

Importance Sampling. In this approach, the weights are first normalized to recover a smooth probability mass function (p.m.f.) over the discrete domain Ω

$$\bar{q}_i^{k+1} = \frac{\lambda_i^{k+1}}{\sum_j \lambda_j^{k+1}}$$

This new distribution \bar{q} is then used to resample a new set of training points $\{X_i\}_{i=1}^N$ from the full collocation set Ω . By focusing the sampling on high-importance regions, the loss can be computed as a standard, unweighted mean squared error on this new, more challenging set of points

$$\mathcal{L}(\theta^{k+1}) = \frac{1}{N} \sum_{i=1}^N r(X_i, \theta^{k+1})^2. \quad (22)$$

Notably, this framework can recover methods similar to residual-based adaptive sampling [21] by setting the potential to $\Phi(x) = x^2 + 1$ and the EMA parameters to $\eta^* = 1$ and $\gamma = 0$.

Importance Weighting. Alternatively, the weights can be used directly in an importance weighting scheme. In this case, the training points $\{X_i\}_{i=1}^N$ are sampled uniformly from Ω . The weights $\{\lambda_i^{k+1}\}$ are then applied directly to the residuals within the loss calculation, creating a weighted objective that reads

$$\mathcal{L}(\theta^{k+1}) = \frac{1}{N} \sum_{i=1}^N [\lambda_i^{k+1} r(X_i, \theta^{k+1})]^2. \quad (23)$$

One might worry that squaring the weights and residual depart from the procedure outlined previously. By an application of Jensen's inequality, one can obtain that squaring the residual (and weights when applicable) corresponds to solving a strictly stronger problem with the added benefits of differentiability.

This framework is also general enough to recover other popular methods. For example, with the potential $\Phi(x) = x^2 + 1$ and specific choices of EMA parameters, it is possible to recover the traditional residual-based adaptive weights [23] and their variations [52, 9]. Similarly, the formulation proposed in [39] can be recovered by constructing the distribution using a locally averaged residual. Our perspective can also be used to interpret other advanced heuristics; for instance, methods that balance the residual decay rate [24] can be

viewed as replacing the simple temporal smoothing via EMA with a more sophisticated, history-aware mechanism for computing the adaptive distribution q^k .

Once the loss $\mathcal{L}(\theta^{k+1})$ is computed using either method, the model parameters can be updated via a line search algorithm, as Adam [59] or BFGS variations such as SSBroyden [16].

4.1.3. Update the regularization parameter

As alluded to before, the choice of the annealing schedule depends on the choice of potential Φ .

Case I: Exponential Potential ($\Phi(x) = e^x$). For this choice, there is no requirements on the choice of ϵ . The particular choice we implemented reads

$$\epsilon^{k+1} = \frac{c \max_{\Omega} r(x; \theta^k)}{\log(2 + k)}.$$

This schedule has several advantages. Using the maximum residual, $\max_{\Omega} |r|$, in the numerator provides a dynamic, problem-dependent characteristic scale for the temperature ϵ . This helps to normalize the magnitude of the residuals relative to the magnitude of the solution itself. The logarithmic term in the denominator ensures a slow and stable decay, such that $\epsilon^k \rightarrow 0$ as $k \rightarrow \infty$, which gradually sharpens the distribution's focus on the largest residuals. In the context of simulated annealing, logarithmic decay is sufficiently slow to guarantee global convergence [71, Theorem 1].

Case II: Quadratic Potential ($\Phi(x) = x^2 + 1$). For this case, the optimality of the distribution q holds under the normalization condition (16), that is,

$$\int_{\Omega} \Phi' \left(\frac{r(x; \theta)}{\epsilon} \right) p(dx) = 1.$$

For this case, the constraint is satisfied by choosing ϵ^k to be the normalizing constant, i.e., the optimal tilt is

$$q^k(dx) = \frac{r(x; \theta^k)}{\int_{\Omega} r(x'; \theta^k) p(dx')} p(dx).$$

This is a consequence of the simple structure of the quadratic potential. Such simplifications can hold for more general polynomial potentials (with additive constants) as well.

4.2. Physics-Informed Neural Networks (PINNs)

In the PINN framework, the goal is to approximate the solution $\bar{u}(x)$ of a PDE or ODE using a representation model $u(\theta, x)$. The training objective ensures that the model satisfies the governing equations and any available data, which may include boundary conditions, initial conditions, or sparse observations.

The total loss function combines the individual loss terms for the governing equations (\mathcal{L}_E), boundary, or initial conditions (\mathcal{L}_B), and, for inverse problems, observational data (\mathcal{L}_D), which reads

$$\mathcal{L} = m_E \mathcal{L}_E + m_B \mathcal{L}_B + m_D \mathcal{L}_D, \tag{24}$$

where m_E, m_B , and m_D are global weights that balance the contribution of each term. The individual loss functions ($\mathcal{L}_E, \mathcal{L}_B, \mathcal{L}_D$) are each computed as described in equation (22) for the importance sampling approach or as in equation (23) for the importance weighting. To ensure the update directions induced by the different loss components are balanced, we employ the self-scaling mechanism presented in [9]. A detailed description of the proposed method is presented in algorithm 1.

4.3. Operator Learning

Neural Operators (NOs) learn mappings between function spaces, approximating a solution operator G_θ that takes an input function, such as a source term f , and maps it to the corresponding solution u [75, 5]. They can also be formulated to propagate a solution in time, taking $u(t_0)$ and returning $u(t_0 + \Delta t)$. While several variations of operators exist, this study focuses on three popular architectures: DeepONet [4], Fourier Neural Operators (FNOs) [5], and the Time-conditioned U-Net [41, 76]. A detailed description of these is provided in Appendix C. The framework described in Section 4.1 can be extended to this case, which requires updating our notation.

Let \mathcal{X} be a space of functions over a domain $\Omega_X \subset \mathbb{R}^{d_x}$, and \mathcal{Y} be a space of functions over $\Omega_Y \subset \mathbb{R}^{d_y}$. The operator of interest is

$$\mathcal{G} : \mathcal{X} \ni v \mapsto \mathcal{G}[v] \in \mathcal{Y}.$$

The goal is to learn a parametric model G_θ that approximates \mathcal{G} . The residual $R : \mathcal{X} \times \Omega_y \rightarrow \mathbb{R}^+$ for this task is defined as the difference between the operator’s prediction and the true solution and reads

$$R(v, x; \theta) = |G_\theta(v)(x) - \mathcal{G}[v](x)|, \tag{25}$$

where $v \in \mathcal{X}$ is an input function and $\mathcal{G}[v]$ is the corresponding true output function evaluated at a point $x \in \Omega_Y$. The training data consists of N_{func} input-output function pairs, $\{v_j, \mathcal{G}[v_j]\}_{j=1}^{N_{\text{func}}}$, where each output function $\mathcal{G}[v_j]$ is evaluated at N discrete points $\{x_i\}_{i=1}^N$. The standard loss is an average over both the function instances and the spatial points:

$$\mathcal{L}(\theta) = \frac{1}{N_{\text{func}}} \sum_{j=1}^{N_{\text{func}}} \frac{1}{N} \sum_{i=1}^N [R(v_j, x_i; \theta)]^2 \tag{26}$$

A single importance sampling or weighting scheme is ill-suited for this problem due to the two distinct levels of discretization (in function space and spatial domains). To address this, we propose a mixed strategy: importance weighting is used for the spatial points within each function, while importance sampling is used for the functions themselves. This is motivated by the fact that many NOs have a fixed spatial discretization, making weighting a natural fit, while the function space offers more flexibility for sampling.

The loss function for a batch of b_u functions is updated as follows

$$\mathcal{L}(\theta) = \frac{1}{b_u} \sum_{j=1}^{b_u} \frac{1}{N} \sum_{i=1}^N [\Lambda_{i,j} R(v_j, x_i; \theta)]^2, \tag{27}$$

where the functions $\{v_j\}_{j=1}^{b_u}$ are sampled from the full set of training functions. The term Λ is a matrix of importance weights, where $\Lambda_{i,j}$ corresponds to point x_i for function v_j . These weights are constructed from a target p.m.f. matrix Q^k constructed based on the choice of potential. For instance when $\Phi(x) = e^x$, $Q^k \in \mathbb{R}^{N \times N_{\text{func}}}$ is defined recursively as follows

$$Q_{i,j}^{k+1}(\theta^k) = \frac{\exp\left(\frac{R(v_j, x_i; \theta^k)}{\epsilon^k}\right)}{\sum_{\ell=1}^N \exp\left(\frac{R(v_j, x_\ell; \theta^k)}{\epsilon^k}\right)}.$$

Note that each column of the matrix Q (for a fixed function j) is a p.m.f. over the spatial points, focusing attention on high-residual regions for that specific function. The weights are then smoothed over time with an EMA

$$\Lambda_{i,j}^{k+1} = \gamma \Lambda_{i,j}^k + \eta^* Q_{i,j}^{k+1}(\theta^k). \quad (28)$$

As in the previous case, we can set the learning rate for stability, for example, by normalizing it as $\eta^* = \eta / \max_j Q_{i,j}$. Note that this choice of η^* achieves a normalization per function which is consistent with our two-level discretization. This EMA formulation has the useful property of keeping the weights bounded. As described in [23], the update rule ensures that the weights are constrained to the interval $\Lambda_{i,j} \in (0, \frac{\eta^*}{1-\gamma})$, which aids in stabilizing the training process.

A key advantage of this framework is that, if $\eta \neq 1 - \gamma$, we can leverage the imbalance on learned spatial weights, $\Lambda_{i,j}$, to construct a sampling distribution over the *functions* themselves. The intuition is that functions with higher overall residuals will naturally accumulate larger Λ values over time. Therefore, we propose the following approach to create a function-level sampling distribution. First, we compute an aggregated importance score s_j for each function by summing its spatial weights

$$s_j = \sum_{i=1}^N \Lambda_{i,j}.$$

These scores are then normalized to create a p.m.f. over the function space:

$$\bar{q}_j = \frac{s_j}{\sum_{\ell=1}^{N_{\text{func}}} s_\ell}.$$

This distribution \bar{q} can then be used to sample the most informative functions v_j for the next training batch. A detailed description of the proposed method is given in Algorithm 2

5. Results

5.1. Physics-Informed Neural Networks

5.1.1. Allen-Cahn Equation

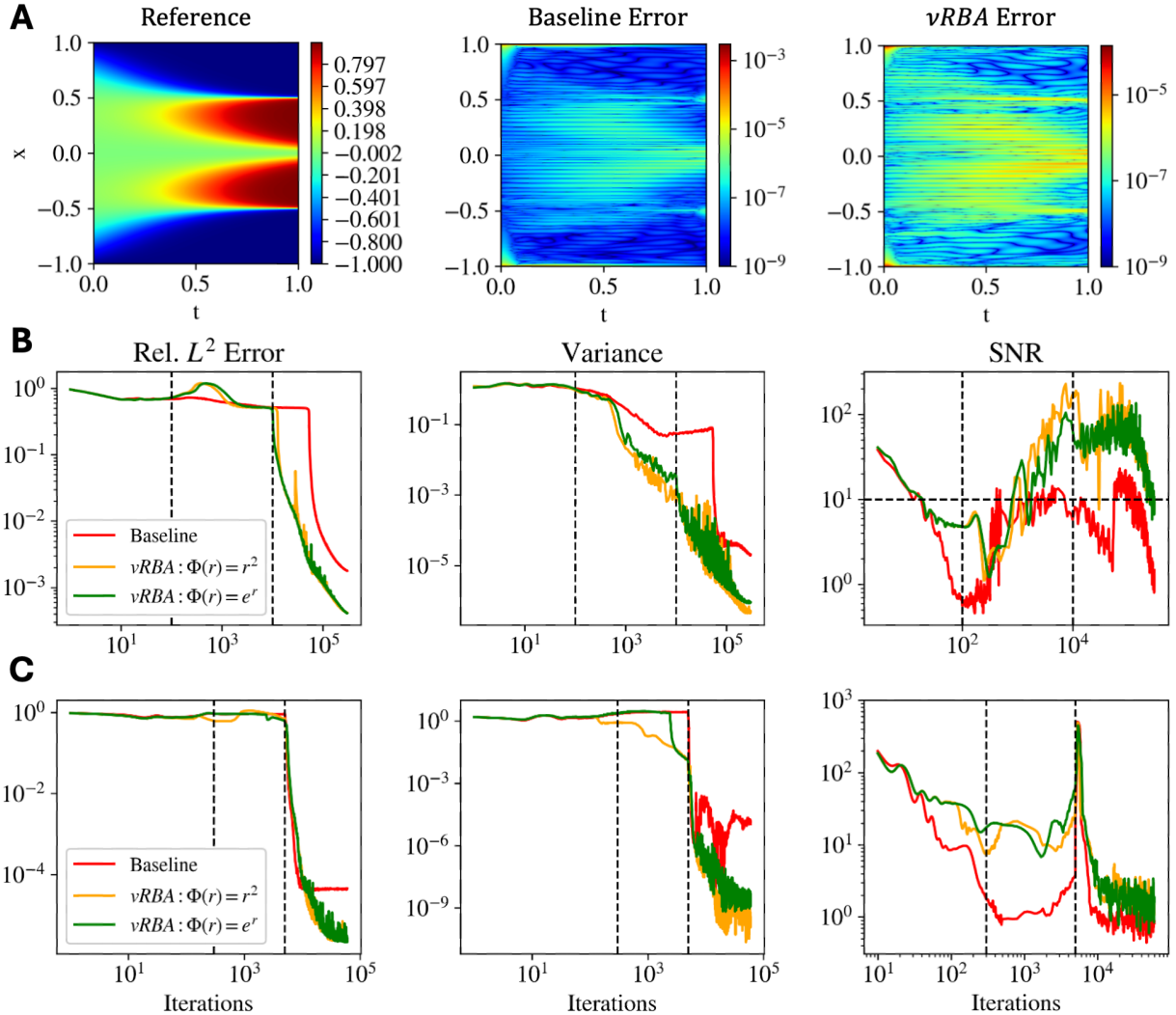


Figure 1: **Allen-Cahn Equation Results.** (A) Comparison of the reference solution, baseline model error, and vRBA ($\Phi(r) = e^r$) error. The baseline’s error is highly concentrated, while vRBA promotes a more uniform distribution, halving the maximum absolute error. (B) Training dynamics with a first-order Adam optimizer, showing relative L^2 error, residual variance, and Signal-to-Noise Ratio (SNR). vRBA converges significantly faster ($\sim 5k$ iterations) than the baseline ($\sim 50k$), substantially reduces residual variance (implying smaller discretization error), and maintains a higher SNR. All models show three learning stages, but vRBA transitions to the productive diffusion phase more rapidly, improving learning dynamics. (C) Training dynamics with a second-order SSBroyden optimizer. Even with an advanced optimizer, vRBA achieves superior performance and faster convergence while the baseline stagnates in a local minimum. vRBA again reduces variance by over three orders of magnitude and maintains a much higher SNR, demonstrating that the adaptive scheme’s benefits are independent of the optimizer.

	Model	N. Params	Optimizer	Time (ms/it)	Rel. L^2 Error
A	Baseline	21318	Adam	4.01	1.77×10^{-3}
	$vRBA : \Phi(r) = r^2$	21318	Adam	4.03	4.08×10^{-4}
	$vRBA : \Phi(r) = e^r$	21318	Adam	4.47	4.14×10^{-4}
B	Baseline	2011	SSBroyden	22.4	4.34×10^{-5}
	$vRBA : \Phi(r) = r^2$	2011	SSBroyden	24.3	2.42×10^{-6}
	$vRBA : \Phi(r) = e^r$	2011	SSBroyden	23.7	2.14×10^{-6}

Table 1: Comparison of models for the Allen-Cahn equation, where baseline models using uniform sampling are benchmarked against the proposed vRBA method. The table presents two distinct scenarios: (a) vRBA applied as an importance weighting strategy for a large network using a first-order optimizer (Adam), and (b) vRBA applied as importance sampling for a compact network using a second-order optimizer (SSBroyden). Notably, using an adaptive method with either an exponential ($\Phi(r) = e^r$) or quadratic ($\Phi(r) = r^2$) potential reduces the relative L^2 error by approximately an order of magnitude, an improvement that holds true even when using a highly optimized second-order method.

The Allen-Cahn equation is a widely recognized benchmark in PINNs due to its challenging characteristics. The 1D Allen-Cahn PDE is defined as:

$$\frac{\partial u}{\partial t} = k \frac{\partial^2 u}{\partial x^2} - 5u(u^2 - 1), \quad (29)$$

where $k = 10^{-4}$. The problem is further defined by the following initial and periodic boundary conditions:

$$u(0, x) = x^2 \cos(\pi x), \quad \forall x \in [-1, 1], \quad (30)$$

$$u(t, x + 1) = u(t, x - 1), \quad \forall t \geq 0 \quad \text{and} \quad x \in [-1, 1]. \quad (31)$$

To provide a broad overview of the influence of vRBA, we split this example into two parts. In the first part, following prior work [54, 23, 77, 36], we use a larger network with Fourier feature embeddings and a first-order Adam optimizer applying vRBA as an importance weighting mechanism. The quantitative results are shown in Table 1(A). The vRBA methods achieve a significantly lower final relative L^2 error, reducing it from 1.77×10^{-3} in the baseline to as low as 4.08×10^{-4} . This more than four-fold improvement is achieved with a negligible increase in computational cost per iteration.

Similarly, Figure 1(B) shows that vRBA significantly accelerates convergence; the vRBA models begin their main convergence phase around 5,000 iterations, whereas the baseline does not start to converge until nearly 50,000 iterations. This enhanced performance can be explained by a twofold mechanism. First, vRBA reduces the variance of the loss estimator, which directly lowers the discretization error. Second, it induces a higher Signal-to-Noise Ratio (SNR), which improves the learning dynamics by enabling a much faster transition to the total diffusion phase. Together, these effects lead to faster convergence and superior model performance.

In the second part, we analyze our model’s performance using the recently introduced SSBroyden optimizer [16], which has been successfully applied in PINNs to obtain highly

accurate results [16, 17, 77]. Following [16], we use Fourier embeddings to encode the periodic boundary conditions. The model parameters are initialized with 5,000 Adam iterations, after which we switch to the SSBroyden optimizer. During the SSBroyden phase, we periodically resample the collocation points every 100 iterations using vRBA as an importance sampling strategy. This approach notably enables the use of mini-batches for training, even with a second-order optimizer.

The results, summarized in Table 1(B), show that this strategy yields a substantial performance gain. The vRBA framework reduces the final relative L^2 error by over an order of magnitude, from 4.34×10^{-5} for the baseline to 2.14×10^{-6} . Figure 1(A) provides a qualitative comparison of the final pointwise error for the SSBroyden experiment, showing the results for the vRBA model with an exponential potential. The baseline model’s error is highly concentrated in specific horizontal bands across the domain. In contrast, the vRBA framework produces a much more spatially uniform error distribution. A significant quantitative gain matches this qualitative improvement: the maximum absolute error is reduced by nearly two orders of magnitude, from approximately 10^{-3} for the baseline to 10^{-5} for the vRBA model.

The learning dynamics in Figure 1(C) offer a more nuanced perspective on how this is achieved. During the initial 5,000 Adam iterations, the model is trapped in the transition stage, and the error for the vRBA models does not decrease, despite a relatively high SNR. The transition to the diffusion phase, where the error rapidly converges, happens immediately upon switching to the SSBroyden optimizer. This transition is signaled by a sharp, initial spike in the SNR, after which the SNR drops to a level lower than it was during the Adam phase. This behavior suggests that the critical event for convergence is the initial escape from the transition phase, rather than simply maintaining a high absolute SNR throughout the entire training process.

Problem	Reference	Optimizer	Enhancements	Rel. L^2 Error
Allen Cahn	[63]	SOAP	PN, FF, WF, CS, LRA	3.48×10^{-6}
	[16]	SSBroyden	RAD, FF	2.20×10^{-6}
	TW	SSBroyden	<i>vRBA</i> ($\Phi = e^r$), FF	2.14×10^{-6}
Burgers	[63]	SOAP	PN, FF, WF, CS, LRA	4.03×10^{-5}
	[16]	SSBroyden	RAD, FF	2.90×10^{-8}
	[17]	SSBroyden	RAD, FF, WLS	1.62×10^{-8}
	TW	SSBroyden	<i>vRBA</i> ($\Phi = e^r$), FF	1.51×10^{-8}

Table 2: State-of-the-art comparison of relative L^2 errors for the Allen-Cahn and Burgers equations, focusing specifically on the performance of various quasi-Newton (second-order) optimization methods. The results from this work (TW) are benchmarked against reported results in recent literature. As described in the preceding sections, the Residual-based Adaptive Distribution (RAD) is a specific type of vRBA that utilizes a quadratic potential without smoothing. The results in this table, therefore, underscore that the combination of an adaptive sampling strategy with a suitable optimizer is critical for achieving high accuracy. Enhancements from the literature are abbreviated as follows: PirateNet (PN) [77], Fourier Features embeddings (FF) [78], Weight Factorization (WF) [79], Causality (CS) [80], Learning Rate Annealing (LRA) [81] and Wolfe Line Search (WLS).

To place our results in context, we compare them against other state-of-the-art methods for the Allen-Cahn equation in Table 2. The comparison focuses on highly accurate solutions obtained with quasi-Newton optimizers. Our proposed method, combining the SSBroyden optimizer with vRBA, yields the most accurate result among the compared methods, achieving a relative L^2 error of 2.14×10^{-6} . It is essential to note that this performance is achieved with a minimal set of enhancements, only Fourier Features and our adaptive sampling framework. This contrasts with other approaches that rely on a more extensive suite of techniques yet yield less accurate results. Furthermore, the table highlights that the previous best result for this problem also uses an adaptive method, RAD. As detailed in our theoretical framework, RAD is a specific instance of vRBA that uses a quadratic potential without smoothing. This underscores our main conclusion: the combination of a powerful optimizer with a principled adaptive sampling strategy like vRBA is the critical factor for achieving the highest accuracy.

5.1.2. Burgers Equation

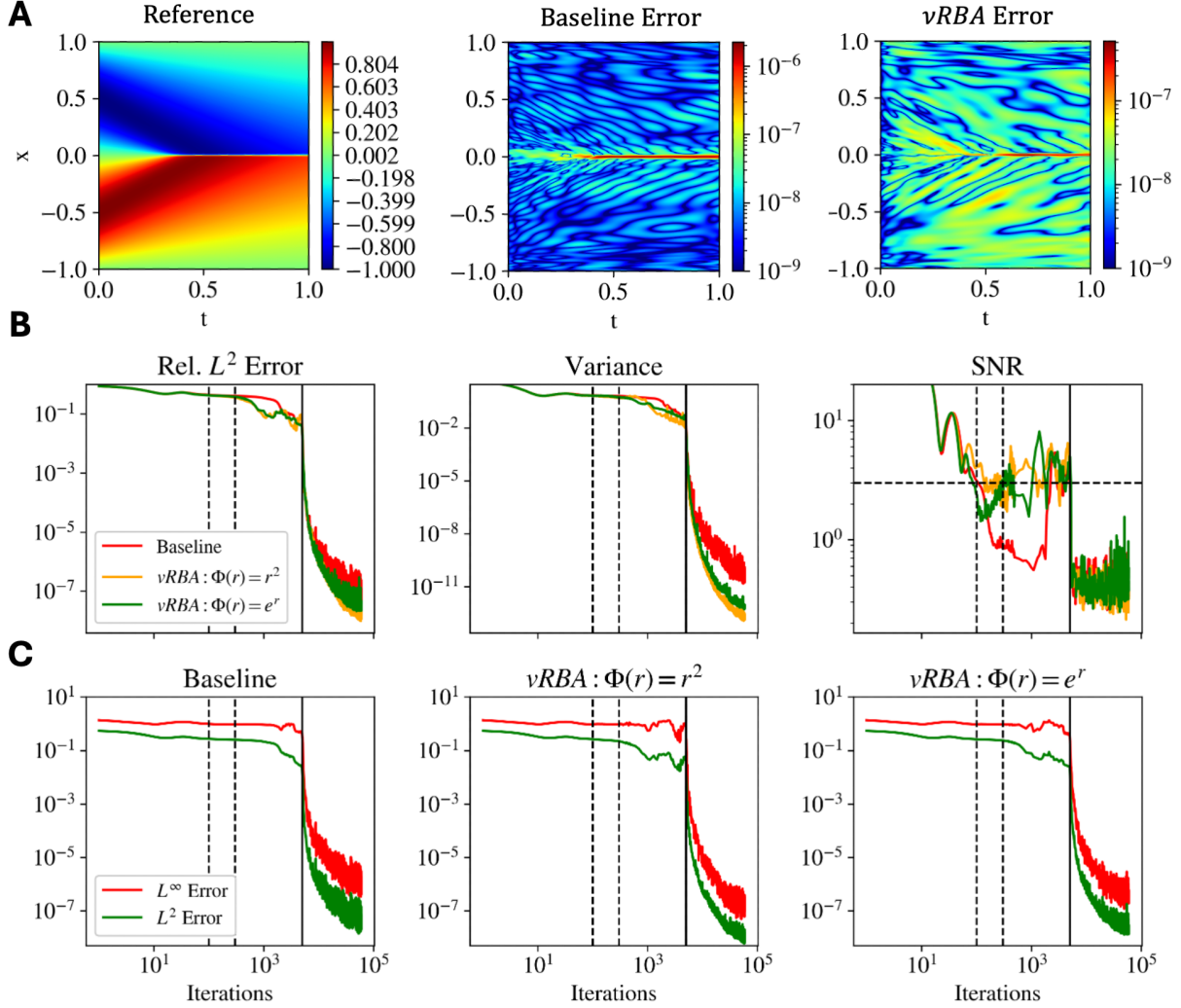


Figure 2: **Burgers' Equation Results.** (A) Comparison of the model prediction, reference solution, and pointwise absolute error. The baseline model's error is highly concentrated along the pseudo-discontinuity (shock front), whereas the vRBA framework successfully distributes the error more uniformly across the spatiotemporal domain, resulting in a significantly lower overall error. (B) Training dynamics showing the convergence of relative L^2 error, residual variance, and SNR with the SSBroyden optimizer. Both vRBA models achieve a lower final relative error and reduce the residual variance by three orders of magnitude. The learning dynamics are notably improved, as evidenced by the higher SNR, with the most pronounced gains occurring within the first 1,000 iterations. (C) Evolution of the L^2 and L^∞ error norms during training. For all methods, the two error norms exhibit similar convergence patterns. Crucially, the L^∞ error consistently provides an upper bound for the L^2 error, visually confirming that its minimization is a stronger convergence criterion.

The Burgers' equation is defined as

$$u_t + uu_x = \nu u_{xx}, \quad (32)$$

where u represents the velocity field, subject to the dynamic viscosity $\nu = 1/(100\pi)$. The initial condition and boundary conditions are described as follows

$$u(0, x) = -\sin(\pi x), \quad \forall x \in \Omega, \quad (33)$$

$$u(t, -1) = u(t, 1) = 0, \quad \forall t \geq 0, \quad (34)$$

defined over the domain $\Omega = (-1, 1) \times (0, 1)$, where $\mathbf{x} = (x, y)$ signifies the spatial coordinates.

Model	N. Params	Optimizer	Time (ms/it)	Rel. L^2 Error
Baseline	2011	SSBroyden	26.1	1.67×10^{-7}
$vRBA : \Phi(r) = r^2$	2011	SSBroyden	28.2	1.74×10^{-8}
$vRBA : \Phi(r) = e^r$	2011	SSBroyden	27.6	1.51×10^{-8}

Table 3: Performance of the vRBA method for the Burgers equation. The vRBA strategies, using either a quadratic ($\Phi(r) = r^2$) or exponential ($\Phi(r) = e^r$) potential, are benchmarked against a baseline model with uniform sampling. All models are trained with the second-order SSBroyden optimizer. The results demonstrate that the vRBA methods improve the final relative L^2 error by an order of magnitude over the baseline, underscoring that an advanced adaptive sampling strategy is critical for achieving high accuracy.

For this example, we follow previous work [16], and enforce the initial and boundary conditions using hard constraints and Fourier embeddings. In this setup, vRBA is again applied as an importance sampling strategy, with the collocation points being resampled every 100 iterations.

The results, presented in Table 3, demonstrate a clear performance advantage for our method, reducing the final relative L^2 error by over an order of magnitude, from 1.67×10^{-7} to 1.51×10^{-8} .

A qualitative view of the final error is provided in Figure 2(A). The baseline model’s error is highly concentrated along the moving shock front, while the vRBA framework produces a much more uniform error distribution. The learning dynamics in Figure 2(B) explain how this is achieved, following the same twofold mechanism observed previously. First, the vRBA models reduce the variance of the loss estimator by three orders of magnitude, which lowers the discretization error. Second, they induce a higher SNR and enable a significantly faster transition to the diffusion phase, resulting in improved learning dynamics and faster convergence. Figure 2(C) further confirms that the L^∞ error norm consistently bounds the L^2 error norm.

Finally, we compare our results to the state of the art in Table 2. Our approach, which combines the SSBroyden optimizer with the vRBA sampling framework, yields the most accurate result among the compared methods. This highlights that a principled adaptive strategy is a key component for pushing the boundaries of accuracy in PINNs.

5.2. Operator Learning

5.2.1. Bubble Growth Dynamics-DeepONet

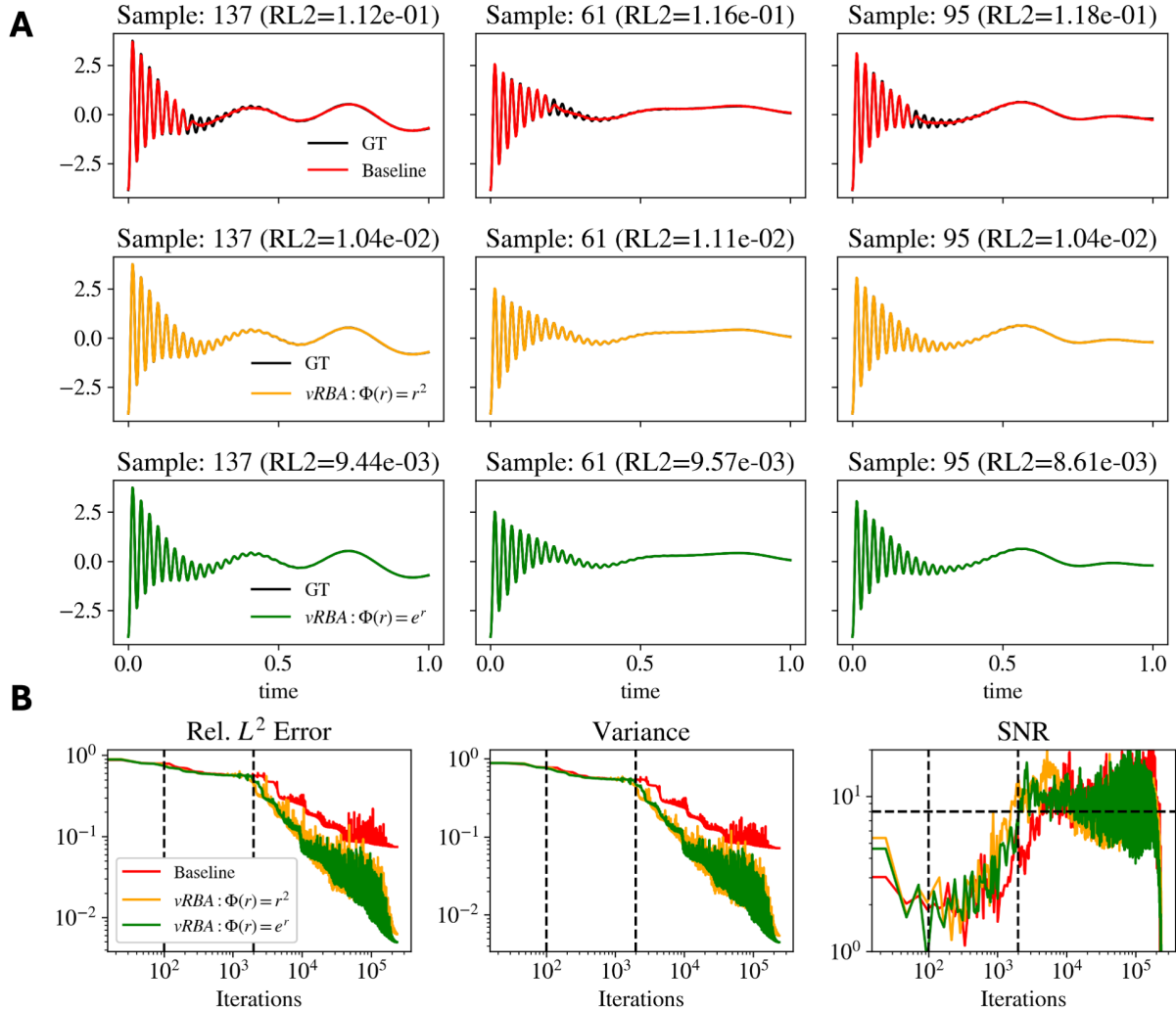


Figure 3: **Bubble Growth Dynamics with DeepONet.** (A) Each column displays a different test function, corresponding to the three examples with the highest error for the baseline model. The rows compare the predictions of the baseline model (top), vRBA with a quadratic potential (middle), and vRBA with an exponential potential (bottom) against the ground truth (GT). The baseline model fails to capture the high-frequency oscillations in the bubble’s dynamics, while both vRBA methods successfully reconstruct these fine-scale features. (B) The plots show the convergence of relative L^2 error, residual variance, and SNR. The vRBA methods achieve a final error that is an order of magnitude lower than the baseline and reduce the variance by two orders of magnitude. This leads to faster and more stable training, evidenced by a consistently higher SNR. The dashed vertical lines mark the learning phases, showing that the vRBA models transition to the productive diffusion stage more rapidly.

We study the dynamics of a single gas bubble in an incompressible liquid governed by the Rayleigh–Plesset (R–P) equation [82], a nonlinear ordinary differential equation describing the evolution of the bubble radius $R(t)$ under a time-varying pressure field $P_\infty(t)$. Under isothermal assumptions and negligible temperature variations, the simplified linearized R–P

equation reads

$$-\frac{\Delta p(t)}{\rho_L} = R_0 \frac{d^2 r}{dt^2} + \frac{4\nu_L}{R_0} \frac{dr}{dt} + \frac{1}{\rho_L R_0} \left(3P_{G0} - \frac{2\gamma}{R_0} \right) r(t), \quad (35)$$

where $r(t) = R(t) - R_0$ is the deviation from the initial bubble radius R_0 , ρ_L is the liquid density, ν_L is the kinematic viscosity, γ is the surface tension, and P_{G0} is the initial gas pressure inside the bubble.

We generate a dataset by numerically solving equation (35) for 1000 independent realizations of the forcing function $\Delta p(t)$, which is constructed as a product of a Gaussian random field and a smooth ramp function, following the procedure in [82]. Specifically, the pressure field is modeled as

$$\Delta p(t) = g(t)s(t), \quad g(t) \sim \mathcal{GP}(\mu, \sigma^2 k(t_1, t_2)),$$

where $k(t_1, t_2)$ is a squared exponential kernel with correlation length ℓ , and $s(t)$ is a smooth ramp used to induce a sharp initial pressure drop.

The data were split into training, validation, and testing subsets in the ratio 80:10:10. Each simulation yields a trajectory of the bubble radius $R(t)$, sampled over a fixed time window with initial condition $R(0) = R_0$, $\dot{R}(0) = 0$. All simulations assume periodic boundary conditions and are performed with parameters corresponding to physical properties of water at room temperature.

To predict the evolution of the bubble radius, we train a DeepONet to learn the mapping from the pressure profile $\Delta p(t)$ to the radius trajectory $R(t)$ [82]. For this and all other operator learning tasks, we apply vRBA using a hybrid strategy of importance weighting in the temporal domain and importance sampling over the function space.

The results, summarized in Table 4, show a dramatic improvement. The vRBA framework reduces the final relative L^2 error by more than an order of magnitude, from 7.41×10^{-2} for the baseline to 4.97×10^{-3} , with only a minor increase in computational cost per iteration. This quantitative gain is reflected in the qualitative predictions shown in Figure 3(A). For challenging test cases, the baseline model fails to capture the high-frequency oscillations in the bubble’s dynamics, whereas both vRBA methods successfully reconstruct these fine-scale features.

The learning dynamics in Figure 3(B) explain this superior performance through the twofold mechanism observed in the PINNs examples. First, vRBA reduces the variance by two orders of magnitude, leading to more stable training. Second, it induces a consistently higher SNR and a much faster transition to the productive diffusion phase, indicating more effective learning.

Problem	Sampling	N. Params	Time (ms/it)	Rel. L^2 Error
BGD (DeepONet)	Baseline	101100	220	7.41×10^{-2}
	$vRBA : \Phi(x) = r^2$	101100	230	6.24×10^{-3}
	$vRBA : \Phi(x) = e^r$	101100	230	4.97×10^{-3}
NS (FNO)	Baseline	1622849	445	5.13×10^{-2}
	$vRBA : \Phi(x) = r^2$	1622849	459	2.37×10^{-2}
	$vRBA : \Phi(x) = e^r$	1622849	460	2.25×10^{-2}
WE (TC-UNet)	Baseline	2432001	810	3.69×10^{-2}
	$vRBA : \Phi(x) = r^2$	2432001	866	1.00×10^{-2}
	$vRBA : \Phi(x) = e^r$	2432001	867	1.05×10^{-2}

Table 4: Performance of the vRBA framework on three operator learning benchmarks: bubble growth dynamics (BGD) solved with a DeepONet, the Navier-Stokes (NS) equations for Kolmogorov flow with an FNO, and the wave equation (WE) with a TC-UNet. In all cases, the vRBA method significantly outperforms the baseline model, which uses uniform sampling. The performance gain is most pronounced for the DeepONet architecture, where vRBA reduces the relative L^2 error by an order of magnitude, with significant improvements also observed for the FNO and TC-UNet models. For these operator learning tasks, all models were trained with the Adam optimizer, and the vRBA method was applied using a hybrid strategy of importance weighting in the spatial domain and importance sampling over the function space.

5.2.2. Navier Stokes-FNO

We consider the two-dimensional unsteady Navier–Stokes equations in vorticity formulation, modeling an incompressible, viscous fluid on the periodic domain $(x, y) \in (0, 2\pi)^2$. The system is driven by a Kolmogorov-type external forcing, as previously studied in [83], and is governed by:

$$\begin{cases} \partial_t \omega + \mathbf{u} \cdot \nabla \omega = \nu \Delta \omega + f(x, y), \\ \nabla \cdot \mathbf{u} = 0, \\ \omega(x, y, 0) = \omega_0(x, y), \end{cases} \quad (36)$$

with viscosity $\nu = 10^{-3}$, and the source term defined as

$$f(x, y) = \chi (\sin(2\pi(x + y)) + \cos(2\pi(x + y))),$$

where $\chi = 0.1$. The Laplacian Δ acts in two spatial dimensions, ω denotes the vorticity, and \mathbf{u} is the velocity.

Initial conditions $\omega_0(x, y)$ are sampled from a Gaussian random field with zero mean and covariance operator $\mathcal{N}(0, 7^{3/2}(-\Delta + 49I)^{-5/2})$. To generate the data, we employ a Fourier-based pseudo-spectral solver introduced in [5]. The simulation output consists of 1000 spatiotemporal vorticity realizations, each on a 512×512 spatial grid, subsequently downsampled to 128×128 for downstream learning tasks.

We partition the dataset into training, validation, and testing subsets in an 80:10:10 ratio. A neural operator model \mathcal{G} is trained to predict evolution of the vorticity field by learning the mapping from the initial condition at $t = 0$ to the interval $t \in (0, 50]$.

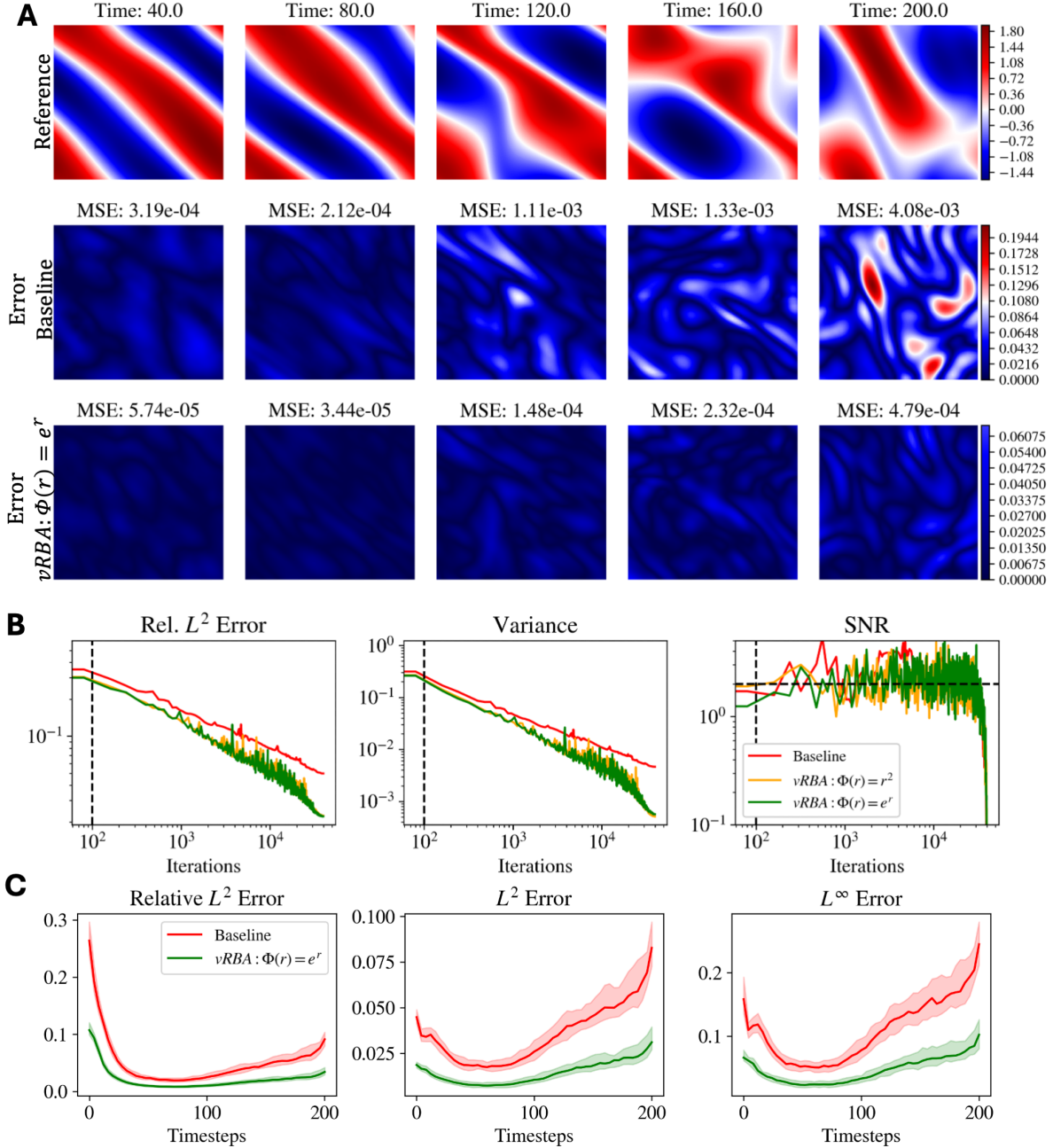


Figure 4: **FNO Performance on 2D Navier-Stokes (Kolmogorov Flow)**. (A) The rows display the reference vorticity field, the pointwise error of the baseline FNO, and the error of the vRBA-enhanced FNO at five temporal snapshots for a test trajectory. At each timestep, the error distribution is much more uniform, and the Mean Squared Error (MSE) is consistently lower than the baseline. (B) Training dynamics showing the convergence of relative L^2 error, residual variance, and SNR. The vRBA methods achieve a lower final error and smaller variance. Interestingly, the SNR for all models remains high throughout training, suggesting the models start in or near the productive diffusion stage, a behavior possibly attributed to the FNO architecture’s Fourier features. (C) These panels show the mean error norms (solid lines) with standard deviation (shaded areas) evaluated over all test trajectories. The vRBA model exhibits both a lower mean error and a smaller standard deviation, indicating more robust and generalizable performance. Crucially, vRBA also shows a much slower rate of error accumulation over time.

For the 2D Navier-Stokes problem, we train a Fourier Neural Operator (FNO) to learn the mapping from an initial vorticity field $\omega_0(x, y)$ to the full spatiotemporal solution $\omega(x, y, t)$.

The vRBA framework again provides a significant performance boost, as shown in Table 4. It more than halves the final relative L^2 error, reducing it from 5.13×10^{-2} to 2.25×10^{-2} , with a negligible impact on the computational time per iteration. The qualitative results in Figure 4(A) are even more striking, showing that the pointwise Mean Squared Error for the vRBA model is often nearly an order of magnitude lower than the baseline at different temporal snapshots.

The analysis of the error accumulation over the test set in Figure 4(C) is particularly important. The vRBA model is not only more accurate on average (lower mean error) but also more robust and generalizable (smaller standard deviation). Most critically, it exhibits a significantly slower rate of error accumulation, a key advantage for long-term, stable predictions.

The training dynamics in Figure 4(B) present a unique behavior. While vRBA still yields a lower final error and reduced variance, the SNR for all models starts and remains high throughout training. This suggests that the FNO architecture, likely due to the strong spectral bias from its built-in Fourier features, begins training in or near the productive diffusion stage, bypassing the typical fitting and transition phases observed in other architectures.

5.2.3. Wave-Equation- TC-UNet

We investigate the propagation of acoustic waves governed by the linear wave equation in heterogeneous media. In 2D, the governing equation is given by:

$$\begin{cases} \partial_t^2 u(\mathbf{x}, t) = c^2(\mathbf{x}) \Delta u(\mathbf{x}, t), & \mathbf{x} \in [0, \pi]^2, t \in [0, 2], \\ u(\mathbf{x}, 0) = u_0(\mathbf{x}), \quad \partial_t u(\mathbf{x}, 0) = 0, & \mathbf{x} \in [0, \pi]^2, \end{cases} \quad (37)$$

where $u(\mathbf{x}, t)$ represents the acoustic pressure at spatial location $\mathbf{x} = (x, y)$, $c(\mathbf{x})$ is the spatially varying wave speed, and Δ denotes the Laplacian operator. We assume fully reflective (homogeneous Dirichlet) boundary conditions throughout the domain.

For the spatially varying wave speed, we set $c(x, y) = 1 + \sin(x) \sin(y)$. The initial pressure profile $u_0(\mathbf{x})$ is modeled as a localized Gaussian source centered at a point \mathbf{x}_c , i.e.,

$$u_0(\mathbf{x}) = \exp\left(-\frac{\|\mathbf{x} - \mathbf{x}_c\|^2}{10}\right),$$

with \mathbf{x}_c sampled randomly on the spatial grid. We solve this system numerically using a second-order finite difference method on a grid with a spatial resolution of 64×64 and generate 1000 simulations corresponding to different realizations of u_0 . The dataset is partitioned into training, validation, and test sets in the ratio 80:10:10. We train a neural operator \mathcal{G} to learn the mapping $u(\mathbf{x}, 0) \mapsto u(\mathbf{x}, t)$ for all $t \in (0, 2]$.

In our final operator learning example, we train a Time-Conditioned U-Net (TC-UNet) to learn the solution operator for the 2D wave equation, mapping an initial pressure profile $u_0(\mathbf{x})$ to the full wave propagation over time $u(\mathbf{x}, t)$.

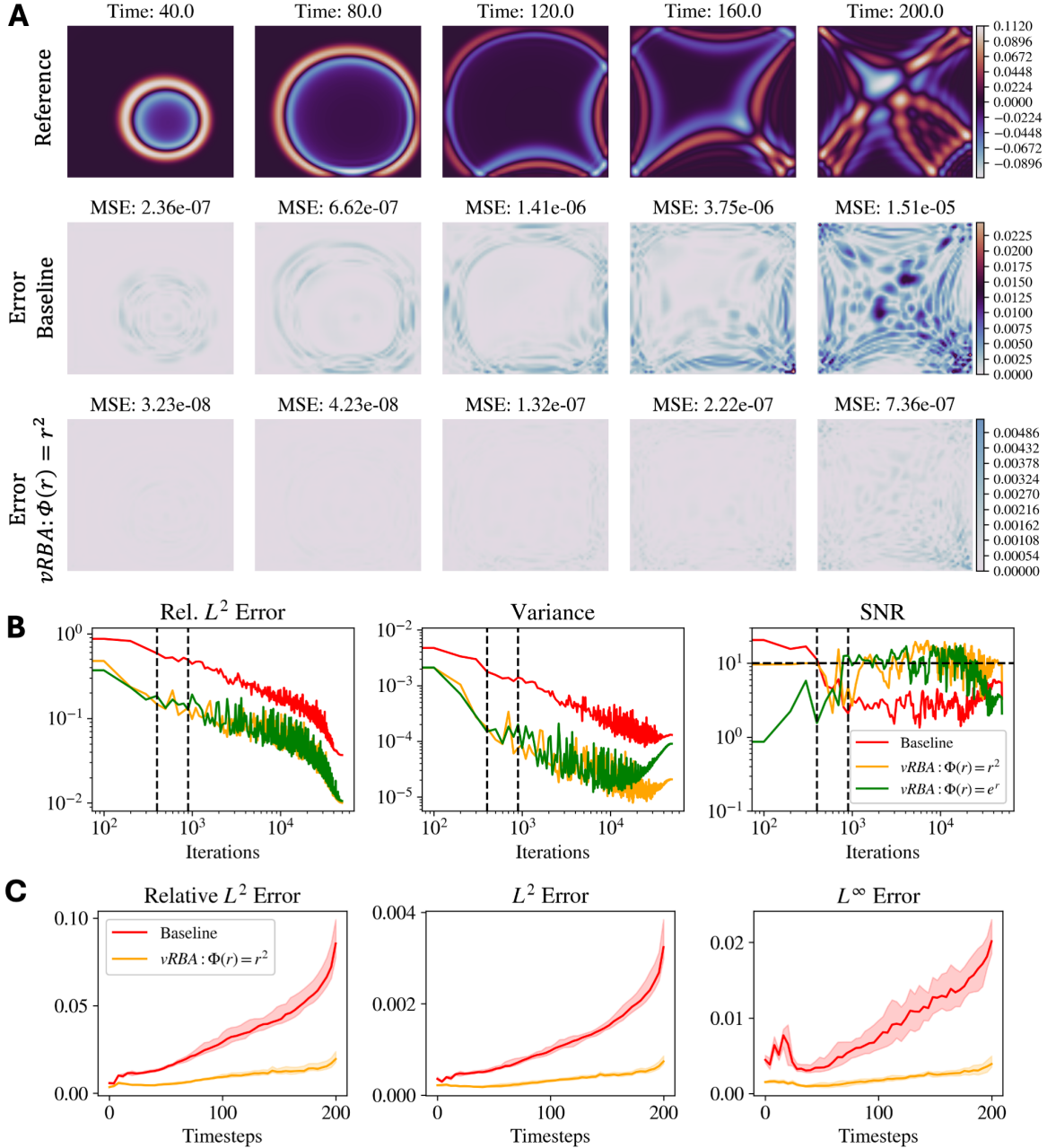


Figure 5: **TC-UNet Performance on the 2D Wave Equation.** (A) The rows show the reference solution, baseline pointwise error, and vRBA pointwise error at five temporal snapshots for a representative trajectory from the test dataset. The vRBA method yields a more uniform error distribution and achieves lower Mean Squared Error (MSE). (B) The plots for relative L^2 error, variance, and SNR demonstrate vRBA’s superior performance during training. Both vRBA models achieve a lower final error and reduced variance, though the variance for the exponential potential increases late in training, possibly due to overfitting. The SNR plot shows the three phases of learning, with the vRBA methods transitioning to the diffusion phase faster. (C) These plots show the mean error norms (solid lines) and standard deviation (shaded areas) evaluated over all trajectories in the test set. The vRBA $\Phi(r) = r^2$ model not only has a lower mean error but also a significantly smaller standard deviation, indicating more robust and generalizable performance. Furthermore, the baseline model’s error accumulates at a much faster rate.

As shown in Table 4, vRBA again delivers a substantial improvement, reducing the final relative L^2 error by a factor of 3.7, from 3.69×10^{-2} down to 1.00×10^{-2} . The qualitative results in Figure 5(A) for a single test trajectory are particularly compelling, showing that the pointwise MSE for the vRBA model is over an order of magnitude smaller than the baseline, and the error is far more spatially uniform.

The analysis over the full test set in Figure 5(C) confirms the method’s effectiveness. The vRBA model is not only more accurate on average but also more robust, as indicated by the smaller standard deviation across all test cases. It also demonstrates a slower rate of error accumulation, a crucial property for predictive accuracy over long time horizons.

The training dynamics in Figure 5(B) mirror the behavior seen in the DeepONet example, showcasing the twofold benefit of vRBA. First, it reduces the variance of the loss estimator, though we note a slight increase late in training for the exponential potential, possibly indicating the onset of overfitting. Second, it induces a higher SNR, allowing the model to transition from the fitting to the diffusion phase more rapidly, which leads to faster and more reliable convergence.

6. Summary and Discussion

In this work, we addressed the largely heuristic nature of residual-based adaptive methods in scientific machine learning. We introduced a unifying variational framework that provides a formal justification and a principled design strategy for these techniques. By leveraging variational representations of integrated-convex functionals, we established a direct link between the form of the adaptive weights or sampling distribution and the primal optimization objective. This connection formally unifies residual-based attention weights (RBA) and residual-based adaptive distribution (RAD) schemes, showing they are different practical implementations of the same underlying principle: optimizing a dual formulation of a chosen primal objective.

The benefits of this framework are manifold and explain the large success of residual-based attention methods from previous studies. It provides a principled origin for heuristics by showing that the choice of potential function dictates the primal optimization objective, such as an exponential potential for L^∞ minimization or a quadratic potential for variance reduction. By promoting a more uniform magnitude for the residuals, vRBA forces the model to capture fine solution details often missed during standard optimization. Furthermore, the framework directly addresses discretization error by reducing the variance of the loss estimator, a benefit we numerically demonstrated to be several orders of magnitude. Moreover, vRBA enhances the learning dynamics; our analysis reveals that vRBA maintains a high signal-to-noise ratio (SNR) of the back-propagated gradients throughout training and transitions to diffusion faster, thereby accelerating convergence.

We demonstrated the efficacy and versatility of vRBA across a range of challenging benchmarks in both PINNs and, notably, operator learning. For the latter, we introduced a hybrid strategy, employing importance sampling over the function space and importance weighting over the spatial domain, which proved particularly effective at reducing the rate of error accumulation. Our empirical results confirmed that vRBA is a critical component for achieving high accuracy, providing substantial improvements even when paired with state-of-the-art second-order optimizers and diverse neural operator architectures.

This work provides a formal basis for the success of residual-based adaptation and opens new avenues for the principled design of effective discretization and optimization strategies. The implications of our variational perspective extend beyond methods that use the residual directly. For instance, the learnable weights proposed in self-adaptive methods, whether treated as trainable parameters or generated by auxiliary networks [22, 54], can be reinterpreted through our framework as a strategy for learning the optimal biasing distribution. This can be viewed as an alternative approach to solving the dual optimization problem, where the distribution is learned rather than derived analytically from a fixed potential. Our framework thus provides a theoretical lens through which an even broader class of adaptive techniques can be unified and analyzed.

Acknowledgements

We acknowledge the support of the NIH grant R01AT012312, MURI/AFOSR FA9550-20-1-0358 project, the DOE-MMICS SEA-CROGS DE-SC0023191 award, and the ONR Vannevar Bush Faculty Fellowship (N00014-22-1-2795).

Data availability

To support reproducibility, the source code for our implementation and data will be publicly available in our [GitHub repository](#) upon acceptance of the manuscript.

References

- [1] M. Raissi, H. Babaei, P. Givi, Deep learning of turbulent scalar mixing, *Physical Review Fluids* 4 (12) (2019) 124501.
- [2] K. Shukla, P. C. Di Leoni, J. Blackshire, D. Sparkman, G. E. Karniadakis, Physics-informed neural network for ultrasound nondestructive quantification of surface breaking cracks, *Journal of Nondestructive Evaluation* 39 (2020) 1–20.
- [3] J. D. Toscano, V. Oommen, A. J. Varghese, Z. Zou, N. Ahmadi Daryakenari, C. Wu, G. E. Karniadakis, From pinns to pikans: Recent advances in physics-informed machine learning, *Machine Learning for Computational Science and Engineering* 1 (1) (2025) 1–43.
- [4] L. Lu, P. Jin, G. E. Karniadakis, DeepOnet: Learning nonlinear operators for identifying differential equations based on the universal approximation theorem of operators, *arXiv preprint arXiv:1910.03193* (2019).
- [5] Z. Li, N. Kovachki, K. Azizzadenesheli, B. Liu, K. Bhattacharya, A. Stuart, A. Anandkumar, Fourier neural operator for parametric partial differential equations, *arXiv preprint arXiv:2010.08895* (2020).
- [6] Z. Liu, Y. Wang, S. Vaidya, F. Ruehle, J. Halverson, M. Soljačić, T. Y. Hou, M. Tegmark, KAN: Kolmogorov-Arnold Networks, *arXiv preprint arXiv:2404.19756* (2024).

- [7] Z. Liu, P. Ma, Y. Wang, W. Matusik, M. Tegmark, KAN 2.0: Kolmogorov-Arnold networks meet science, arXiv preprint arXiv:2408.10205 (2024).
- [8] Y. Wang, J. W. Siegel, Z. Liu, T. Y. Hou, On the expressiveness and spectral bias of KANs, arXiv preprint arXiv:2410.01803 (2024).
- [9] J. D. Toscano, L.-L. Wang, G. E. Karniadakis, Kkans: Kurkova-kolmogorov-arnold networks and their learning dynamics, *Neural Networks* (2025) 107831.
- [10] D. Stenkin, V. Gorbachenko, Mathematical modeling on a physics-informed radial basis function network, *Mathematics* 12 (2) (2024) 241.
- [11] Z. Uddin, S. Ganga, R. Asthana, W. Ibrahim, Wavelets based physics informed neural networks to solve non-linear differential equations, *Scientific Reports* 13 (1) (2023) 2882.
- [12] C. Wu, A. J. Varghese, V. Oommen, G. E. Karniadakis, Gpt vs human for scientific reviews: A dual source review on applications of chatgpt in science, arXiv preprint arXiv:2312.03769 (2023).
- [13] L. Song, J. D. Toscano, L.-L. Wang, Explicit construction of approximate kolmogorov-arnold superpositions with c2-smoothness, arXiv preprint arXiv:2508.04392 (2025).
- [14] Z. Hu, K. Shukla, G. E. Karniadakis, K. Kawaguchi, Tackling the curse of dimensionality with physics-informed neural networks, *Neural Networks* 176 (2024) 106369.
- [15] A. Jnini, F. Vella, M. Zeinhofer, Gauss-Newton Natural Gradient Descent for Physics-Informed Computational Fluid Dynamics, arXiv preprint arXiv:2402.10680 (2024).
- [16] J. F. Urbán, P. Stefanou, J. A. Pons, Unveiling the optimization process of Physics Informed Neural Networks: How accurate and competitive can PINNs be?, arXiv preprint arXiv:2405.04230 (2024).
- [17] E. Kiyani, K. Shukla, J. F. Urbán, J. Darbon, G. E. Karniadakis, Optimizing the optimizer for physics-informed neural networks and kolmogorov-arnold networks, *Computer Methods in Applied Mechanics and Engineering* 446 (2025) 118308.
- [18] M. Zeinhofer, R. Masri, K.-A. Mardal, A unified framework for the error analysis of physics-informed neural networks, *IMA Journal of Numerical Analysis* (2024) drae081.
- [19] N. Sukumar, A. Srivastava, Exact imposition of boundary conditions with distance functions in physics-informed deep neural networks, *Computer Methods in Applied Mechanics and Engineering* 389 (2022) 114333.
- [20] L. Lu, X. Meng, Z. Mao, G. E. Karniadakis, DeepXDE: A deep learning library for solving differential equations, *SIAM Review* 63 (1) (2021) 208–228.
- [21] C. Wu, M. Zhu, Q. Tan, Y. Kartha, L. Lu, A comprehensive study of non-adaptive and residual-based adaptive sampling for physics-informed neural networks, *Computer Methods in Applied Mechanics and Engineering* 403 (2023) 115671.

- [22] L. D. McClenny, U. M. Braga-Neto, Self-adaptive physics-informed neural networks, *Journal of Computational Physics* 474 (2023) 111722.
- [23] S. J. Anagnostopoulos, J. D. Toscano, N. Stergiopoulos, G. E. Karniadakis, Residual-based attention in physics-informed neural networks, *Computer Methods in Applied Mechanics and Engineering* 421 (2024) 116805.
- [24] W. Chen, A. A. Howard, P. Stinis, Self-adaptive weights based on balanced residual decay rate for physics-informed neural networks and deep operator networks, *Journal of Computational Physics* (2025) 114226.
- [25] S. Basir, I. Senocak, An adaptive augmented Lagrangian method for training physics and equality constrained artificial neural networks, *arXiv preprint arXiv:2306.04904* (2023).
- [26] S. Basir, I. Senocak, Physics and equality constrained artificial neural networks: Application to forward and inverse problems with multi-fidelity data fusion, *Journal of Computational Physics* 463 (2022) 111301.
- [27] Q. Hu, S. Basir, I. Senocak, Conditionally adaptive augmented lagrangian method for physics-informed learning of forward and inverse problems using artificial neural networks, *arXiv preprint arXiv:2508.15695* (2025).
- [28] A. Daw, J. Bu, S. Wang, P. Perdikaris, A. Karpatne, Rethinking the importance of sampling in physics-informed neural networks, *arXiv preprint arXiv:2207.02338* (2022).
- [29] W. Gao, C. Wang, Active learning based sampling for high-dimensional nonlinear partial differential equations, *Journal of Computational Physics* 475 (2023) 111848.
- [30] H. Son, S. W. Cho, H. J. Hwang, Enhanced physics-informed neural networks with augmented lagrangian relaxation method (AL-PINNs), *Neurocomputing* (2023) 126424.
- [31] J. D. Toscano, C. Wu, A. Ladrón-de Guevara, T. Du, M. Nedergaard, D. H. Kelley, G. E. Karniadakis, K. A. Boster, Inferring in vivo murine cerebrospinal fluid flow using artificial intelligence velocimetry with moving boundaries and uncertainty quantification, *Interface Focus* 14 (6) (2024) 20240030.
- [32] I. Ramirez, J. Pinoa, D. Pardob, M. Sanz, L. del Rio, A. Ortize, K. Morozovskaf, J. I. Aizpuruag, Residual-based attention physics-informed neural networks for spatio-temporal ageing assessment of transformers operated in renewable power plants, *arXiv preprint arXiv:2405.06443* (2024).
- [33] S. Wang, P. Zhao, T. Song, Aspinn: An asymptotic strategy for solving singularly perturbed differential equations, *arXiv preprint arXiv:2409.13185* (2024).
- [34] I. Ramirez, J. Pino, D. Pardo, M. Sanz, L. del Rio, A. Ortiz, K. Morozovska, J. I. Aizpuru, Residual-based attention physics-informed neural networks for spatio-temporal ageing assessment of transformers operated in renewable power plants, *Engineering Applications of Artificial Intelligence* 139 (2025) 109556.

- [35] S. Wang, P. Zhao, Q. Ma, T. Song, General-kindred physics-informed neural network to the solutions of singularly perturbed differential equations, *Physics of Fluids* 36 (11) (2024).
- [36] W. Chen, A. A. Howard, P. Stinis, Self-adaptive weights based on balanced residual decay rate for physics-informed neural networks and deep operator networks, *Journal of Computational Physics* (2025) 114226.
- [37] S. Rigas, M. Papachristou, T. Papadopoulos, F. Anagnostopoulos, G. Alexandridis, Adaptive training of grid-dependent physics-informed Kolmogorov-Arnold networks, *IEEE Access* (2024).
- [38] C. Wu, J. D. Toscano, K. Shukla, Y. Chen, A. Shahmohammadi, E. Raymond, T. Toupay, N. Nazemifard, C. Papageorgiou, G. E. Karniadakis, Fmenets: Flow, material, and energy networks for non-ideal plug flow reactor design, *arXiv preprint arXiv:2505.20300* (2025).
- [39] C. Si, M. Yan, Convolution-weighting method for the physics-informed neural network: A primal-dual optimization perspective, *arXiv preprint arXiv:2506.19805* (2025).
- [40] J. D. Toscano, Y. Guo, Z. Wang, Y. Mori, M. Vaezi, G. E. Karniadakis, K. A. Boster, D. H. Kelley, Mr-aiiv reveals in-vivo brain-wide fluid flow with physics-informed ai, *bioRxiv* (2025) 2025–07.
- [41] O. Ovadia, V. Oommen, A. Kahana, A. Peyvan, E. Turkel, G. E. Karniadakis, Real-time inference and extrapolation with time-conditioned unet: Applications in hypersonic flows, incompressible flows, and global temperature forecasting, *Computer Methods in Applied Mechanics and Engineering* 441 (2025) 117982.
- [42] A. R. Barron, Universal approximation bounds for superpositions of a sigmoidal function, *IEEE Transactions on Information Theory* 39 (3) (1993) 930–945.
- [43] J. Park, I. W. Sandberg, Universal approximation using radial-basis-function networks, *Neural Computation* 3 (2) (1991) 246–257.
- [44] K. Hornik, Approximation capabilities of multilayer feedforward networks, *Neural Networks* 4 (2) (1991) 251–257.
- [45] K. Tang, X. Wan, C. Yang, DAS: A deep adaptive sampling method for solving partial differential equations, *arXiv preprint arXiv:2112.14038* (2021).
- [46] W. Peng, W. Zhou, X. Zhang, W. Yao, Z. Liu, Rang: A residual-based adaptive node generation method for physics-informed neural networks, *arXiv preprint arXiv:2205.01051* (2022).
- [47] S. Zeng, Z. Zhang, Q. Zou, Adaptive deep neural networks methods for high-dimensional partial differential equations, *Journal of Computational Physics* 463 (2022) 111232.

- [48] J. M. Hanna, J. V. Aguado, S. Comas-Cardona, R. Askri, D. Borzacchiello, Residual-based adaptivity for two-phase flow simulation in porous media using physics-informed neural networks, *Computer Methods in Applied Mechanics and Engineering* 396 (2022) 115100.
- [49] S. Subramanian, R. M. Kirby, M. W. Mahoney, A. Gholami, Adaptive self-supervision algorithms for physics-informed neural networks, in: *ECAI 2023*, IOS Press, 2023, pp. 2234–2241.
- [50] M. A. Nabian, R. J. Gladstone, H. Meidani, Efficient training of physics-informed neural networks via importance sampling, *Computer-Aided Civil and Infrastructure Engineering* 36 (8) (2021) 962–977.
- [51] B. Zapf, J. Haubner, M. Kuchta, G. Ringstad, P. K. Eide, K.-A. Mardal, Investigating molecular transport in the human brain from MRI with physics-informed neural networks, *Scientific Reports* 12 (1) (2022) 15475.
- [52] J. D. Toscano, T. Käufer, Z. Wang, M. Maxey, C. Cierpka, G. E. Karniadakis, Aivt: Inference of turbulent thermal convection from measured 3d velocity data by physics-informed kolmogorov-arnold networks, *Science advances* 11 (19) (2025) eads5236.
- [53] A. Daw, J. Bu, S. Wang, P. Perdikaris, A. Karpatne, Mitigating propagation failures in physics-informed neural networks using retain-resample-release (r3) sampling, *arXiv preprint arXiv:2207.02338* (2022).
- [54] G. Zhang, H. Yang, F. Zhu, Y. Chen, et al., DASA-PINNs: Differentiable Adversarial Self-Adaptive Pointwise Weighting Scheme for Physics-Informed Neural Networks, *SSRN* (2023).
- [55] S. Basir, Investigating and mitigating failure modes in physics-informed neural networks (PINNs), *arXiv preprint arXiv:2209.09988* (2022).
- [56] Y. Song, H. Wang, H. Yang, M. L. Taccari, X. Chen, Loss-attentional physics-informed neural networks, *Journal of Computational Physics* 501 (2024) 112781.
- [57] K. Shukla, J. D. Toscano, Z. Wang, Z. Zou, G. E. Karniadakis, A comprehensive and FAIR comparison between MLP and KAN representations for differential equations and operator networks, *Computer Methods in Applied Mechanics and Engineering* 431 (2024) 117290.
- [58] I. Ramirez, J. Pino, D. Pardo, M. Sanz, L. del Rio, A. Ortiz, K. Morozovska, J. I. Aizpuru, Residual-based attention physics-informed neural networks for efficient spatio-temporal lifetime assessment of transformers operated in renewable power plants, *arXiv preprint arXiv:2405.06443* (2024).
- [59] D. P. Kingma, J. Ba, Adam: A method for stochastic optimization, *arXiv preprint arXiv:1412.6980* (2014).

- [60] T. Schaul, S. Zhang, Y. LeCun, No more pesky learning rates, in: International conference on machine learning, PMLR, 2013, pp. 343–351.
- [61] S. J. Anagnostopoulos, J. D. Toscano, N. Stergiopoulos, G. E. Karniadakis, Learning in PINNs: Phase transition, total diffusion, and generalization, arXiv preprint arXiv:2403.18494 (2024).
- [62] N. Tishby, F. C. Pereira, W. Bialek, The information bottleneck method, arXiv preprint physics/0004057 (2000).
- [63] S. Wang, A. K. Bhartari, B. Li, P. Perdikaris, Gradient alignment in physics-informed neural networks: A second-order optimization perspective, arXiv preprint arXiv:2502.00604 (2025).
- [64] R. Shwartz-Ziv, N. Tishby, Opening the black box of deep neural networks via information, arXiv preprint arXiv:1703.00810 (2017).
- [65] A. Dembo, O. Zeitouni, Large Deviations Techniques and Applications, Vol. 38, Springer Science & Business Media, 2009.
- [66] P. Dupuis, R. S. Ellis, A weak convergence approach to the theory of large deviations, John Wiley & Sons, 2011.
- [67] A. Budhiraja, P. Dupuis, Analysis and approximation of rare events, Representations and Weak Convergence Methods. Series Prob. Theory and Stoch. Modelling 94 (2019) 8.
- [68] A. Alberts, I. Billionis, Physics-informed information field theory for modeling physical systems with uncertainty quantification, Journal of Computational Physics 486 (2023) 112100.
- [69] V. Černý, Thermodynamical approach to the traveling salesman problem: An efficient simulation algorithm, Journal of optimization theory and applications 45 (1) (1985) 41–51.
- [70] S. Kirkpatrick, C. D. Gelatt Jr, M. P. Vecchi, Optimization by simulated annealing, science 220 (4598) (1983) 671–680.
- [71] S. Geman, C.-R. Hwang, Diffusions for global optimization, SIAM Journal on Control and Optimization 24 (5) (1986) 1031–1043.
- [72] J. Birrell, P. Dupuis, M. A. Katsoulakis, Y. Pantazis, L. Rey-Bellet, (f, gamma)-divergences: Interpolating between f-divergences and integral probability metrics, Journal of machine learning research 23 (39) (2022) 1–70.
- [73] A. Fiorenza, An inequality for jensen means, Nonlinear Analysis: Theory, Methods & Applications 16 (2) (1991) 191–198.

- [74] A. Vaswani, N. Shazeer, N. Parmar, J. Uszkoreit, L. Jones, A. N. Gomez, L. Kaiser, I. Polosukhin, Attention is all you need, *Advances in Neural Information Processing Systems* 30 (2017).
- [75] L. Lu, P. Jin, G. Pang, Z. Zhang, G. E. Karniadakis, Learning nonlinear operators via DeepONet based on the universal approximation theorem of operators, *Nature machine intelligence* 3 (3) (2021) 218–229.
- [76] J. K. Gupta, J. Brandstetter, Towards multi-spatiotemporal-scale generalized pde modeling, *arXiv preprint arXiv:2209.15616* (2022).
- [77] S. Wang, B. Li, Y. Chen, P. Perdikaris, PirateNets: Physics-informed Deep Learning with Residual Adaptive Networks, *arXiv preprint arXiv:2402.00326* (2024).
- [78] S. Wang, H. Wang, P. Perdikaris, On the eigenvector bias of Fourier feature networks: From regression to solving multi-scale PDEs with physics-informed neural networks, *arXiv preprint arXiv:2012.10047* (2020).
- [79] S. Wang, H. Wang, J. H. Seidman, P. Perdikaris, Random weight factorization improves the training of continuous neural representations, *arXiv preprint arXiv:2210.01274* (2022).
- [80] S. Wang, S. Sankaran, P. Perdikaris, Respecting causality is all you need for training physics-informed neural networks, *arXiv preprint arXiv:2203.07404* (2022).
- [81] S. Wang, Y. Teng, P. Perdikaris, Understanding and mitigating gradient flow pathologies in physics-informed neural networks, *SIAM Journal on Scientific Computing* 43 (5) (2021) A3055–A3081.
- [82] C. Lin, Z. Li, L. Lu, S. Cai, M. Maxey, G. E. Karniadakis, Operator learning for predicting multiscale bubble growth dynamics, *The Journal of Chemical Physics* 154 (10) (2021).
- [83] G. J. Chandler, R. R. Kerswell, Invariant recurrent solutions embedded in a turbulent two-dimensional kolmogorov flow, *Journal of Fluid Mechanics* 722 (2013) 554–595.
- [84] X. Nguyen, M. J. Wainwright, M. I. Jordan, Estimating divergence functionals and the likelihood ratio by convex risk minimization, *IEEE Transactions on Information Theory* 56 (11) (2010) 5847–5861.
- [85] T. Chen, H. Chen, Universal approximation to nonlinear operators by neural networks with arbitrary activation functions and its application to dynamical systems, *IEEE transactions on neural networks* 6 (4) (1995) 911–917.
- [86] E. Kiyani, M. Manav, N. Kadivar, L. De Lorenzis, G. E. Karniadakis, Predicting crack nucleation and propagation in brittle materials using deep operator networks with diverse trunk architectures, *Computer Methods in Applied Mechanics and Engineering* 441 (2025) 117984.

- [87] A. Peyvan, V. Oommen, A. D. Jagtap, G. E. Karniadakis, Riemannonets: Interpretable neural operators for riemann problems, *Computer Methods in Applied Mechanics and Engineering* 426 (2024) 116996.
- [88] V. Oommen, K. Shukla, S. Goswami, R. Dingreville, G. E. Karniadakis, Learning two-phase microstructure evolution using neural operators and autoencoder architectures, *npj Computational Materials* 8 (1) (2022) 190.
- [89] C. Lin, M. Maxey, Z. Li, G. E. Karniadakis, A seamless multiscale operator neural network for inferring bubble dynamics, *Journal of Fluid Mechanics* 929 (2021) A18.
- [90] T. Kurth, S. Subramanian, P. Harrington, J. Pathak, M. Mardani, D. Hall, A. Miele, K. Kashinath, A. Anandkumar, Fourcastnet: Accelerating global high-resolution weather forecasting using adaptive fourier neural operators, in: *Proceedings of the platform for advanced scientific computing conference, 2023*, pp. 1–11.
- [91] A. Kashefi, T. Mukerji, A novel fourier neural operator framework for classification of multi-sized images: Application to three dimensional digital porous media, *Physics of Fluids* 36 (5) (2024).
- [92] Z. Li, W. Peng, Z. Yuan, J. Wang, Fourier neural operator approach to large eddy simulation of three-dimensional turbulence, *Theoretical and Applied Mechanics Letters* 12 (6) (2022) 100389.
- [93] E. Perez, F. Strub, H. De Vries, V. Dumoulin, A. Courville, Film: Visual reasoning with a general conditioning layer, in: *Proceedings of the AAAI conference on artificial intelligence*, Vol. 32, 2018.
- [94] S. Khodakarami, V. Oommen, A. Bora, G. E. Karniadakis, Mitigating spectral bias in neural operators via high-frequency scaling for physical systems, *arXiv preprint arXiv:2503.13695* (2025).
- [95] V. Oommen, A. Bora, Z. Zhang, G. E. Karniadakis, Integrating neural operators with diffusion models improves spectral representation in turbulence modeling, *arXiv preprint arXiv:2409.08477* (2024).
- [96] V. Oommen, A. E. Robertson, D. Diaz, C. Alleman, Z. Zhang, A. D. Rollett, G. E. Karniadakis, R. Dingreville, Equilibrium conserving neural operators for super-resolution learning, *arXiv preprint arXiv:2504.13422* (2025).
- [97] S. Wang, H. Wang, P. Perdikaris, On the eigenvector bias of Fourier feature networks: From regression to solving multi-scale PDEs with physics-informed neural networks, *Computer Methods in Applied Mechanics and Engineering* 384 (2021) 113938.

Appendix A. Representation of divergences

The derivation of vRBA uses several variational formulas of statistical divergences and related functionals. The goal of this appendix is to review the various representations used to derive vRBA with notation consistent with the manuscript.

The first is the Laplace principle, which rewrites the maximum as integration against increasingly singular measures. While the result is well-known in the context of large deviations, e.g., [65, Theorem 4.3.1] or [67, Theorem 1.5], the statement as presented is difficult to find, so we provide the proof for completeness.

Proposition Appendix A.1. *Let $r : \Omega \rightarrow \mathbb{R}$ be a bounded, measurable function and let $p \in \mathcal{P}(\Omega)$ be a probability measure. Let*

$$M = \inf \{m \in \mathbb{R} : p(x \in \Omega : r(x) \leq m) = 1\}$$

be the essential supremum of r . Then, we have

$$M = \sup_{\epsilon > 0} \epsilon \log \int_{\Omega} e^{r(x)/\epsilon} p(dx) = \lim_{\epsilon \rightarrow 0} \epsilon \log \int_{\Omega} e^{r(x)/\epsilon} p(dx).$$

Proof. First, observe that

$$\epsilon \log \int_{\Omega} e^{r(x)/\epsilon} p(dx) \leq \epsilon \log \int_{\Omega} e^{M/\epsilon} p(dx) = M$$

for each $\epsilon > 0$. Therefore, the problem reduces to proving a matching lower bound. We first prove the statement for the case where p is supported on finitely many points, then proceed via approximation.

Finite support. Without loss of generality, we can reduce the problem to showing for $a, b \in \mathbb{R}$ and $a > b$,

$$\lim_{\epsilon \rightarrow 0} \epsilon \log (e^{a/\epsilon} + e^{b/\epsilon}) = a.$$

This follows from rewriting

$$\epsilon \log (e^{a/\epsilon} + e^{b/\epsilon}) = \epsilon \log (e^{a/\epsilon} (1 + e^{(b-a)/\epsilon})) = a + \epsilon \log (1 + e^{(b-a)/\epsilon})$$

and the convergence follows from $b - a < 0$.

Approximation. Without loss of generality, shift and scale r so that $0 \leq r \leq 1$ and $M = 1$. Fix $k \in \mathbb{N}$ and define a partition (up to measure-zero sets)

$$\Omega = \bigcup_{m=0}^{k-1} A_m \quad \text{where} \quad A_m = \left\{ x \in \Omega : \frac{m}{k} \leq r(x) \leq \frac{m+1}{k} \right\}.$$

Then, we can partition the integral:

$$\begin{aligned} \epsilon \log \int_{\Omega} e^{r(x)/\epsilon} p(dx) &= \epsilon \log \left(\sum_{m=0}^{k-1} \int_{A_m} e^{r(x)/\epsilon} p(dx) \right) \\ &\geq \epsilon \log \left(\sum_{m=0}^{k-1} p(A_m) e^{m/k\epsilon} \right) \\ &\rightarrow \left(1 - \frac{1}{k} \right) \quad \text{as } \epsilon \rightarrow 0, \end{aligned}$$

where the last equality is by the convergence in the finite-support case. Finally, taking increasing fine partitions, i.e., sending $k \rightarrow \infty$, completes the proof. \square

Complementary to the Laplace principle, the Gibbs variational formula gives a representation for the log-integrated-exponentials—also known as the log-partition function.

Proposition Appendix A.2. *Let $r : \Omega \rightarrow \mathbb{R}$ be bounded and continuous and $p \in \mathcal{P}(\Omega)$ be a probability measure. Then, the variational formula holds:*

$$\log \int_{\Omega} e^{r(x)} p(dx) = \sup_{q \in \mathcal{P}(\Omega)} \left\{ \int_{\Omega} r(x) q(dx) - \mathbf{H}(q|p) \right\}$$

where \mathbf{H} denotes the relative entropy (defined in (11)). Moreover, the optimizer $q^* \in \mathcal{P}(\Omega)$ that achieves the supremum takes the form

$$q^*(dx) = \frac{e^{r(x)}}{\int_{\Omega} e^{r(x)} p(dx)} p(dx).$$

A proof can be found in, for example, [67, Proposition 2.2]. It consists of two steps: first, showing that the identified q^* achieves equality. Then, decompose the log-likelihood-ratio into ones with respect to the optimizer q^* allows one to use the non-negativity of relative entropy to conclude.

In fact, the Gibbs variational principle is only one part of a duality with the log-partition function. This is known as the Donsker-Varadhan representation, e.g., [67, Lemma 2.4], which gives a representation of the relative entropy as the Legendre-Fenchel transform of the log-partition function:

$$\mathbf{H}(p|q) = \sup_{r \in \mathcal{M}_b(\Omega; \mathbb{R})} \left\{ \int_{\Omega} r(x) q(dx) - \log \int_{\Omega} e^{r(x)} p(dx) \right\}.$$

The set $\mathcal{M}_b(\Omega; \mathbb{R})$ denotes the set of bounded measurable functionals $r : \Omega \rightarrow \mathbb{R}$. A similar duality theory was established in [72].

Proposition Appendix A.3. *Let $r : \Omega \rightarrow \mathbb{R}$ be bounded and measurable and let $p \in \mathcal{P}(\Omega)$ be a probability measure. Let $\Phi : \mathbb{R} \rightarrow \mathbb{R}$ be convex, bounded from below, and superlinear. Then, we have:*

1. a generalized Gibbs variational formula:

$$\inf_{\nu \in \mathbb{R}} \left\{ \nu + \int_{\Omega} \Phi(r(x) - \nu) p(dx) \right\} = \sup_{q \in \mathcal{P}(\Omega)} \left\{ \int_{\Omega} r(x) q(dx) + \mathbf{D}_{\Phi^*}(q|p) \right\};$$

2. when r additionally satisfies

$$\int_{\Omega} \Phi'(r(x)) p(dx) = 1$$

where Φ' is any element in the subdifferential of Φ , then the optimal ν is zero and

$$\int_{\Omega} \Phi(r(x)) p(dx) = \sup_{q \in \mathcal{P}(\Omega)} \left\{ \int_{\Omega} r(x) q(dx) + \mathbf{D}_{\Phi^*}(q|p) \right\}$$

with equality achieved when

$$q(dx) = \Phi'(r(x)) p(dx).$$

Proof. The first item follows from [72, Corollary 58]. The proof is involved and will not be reproduced here.

The second item follows first from a Donsker-Varadhan-type representation of Φ -divergences, which can be found in, e.g., [84, Lemma 1]. By Fenchel-Young,

$$\mathbf{D}_{\Phi^*}(q|p) = \int_{\Omega} \Phi^* \left(\frac{dq}{dp}(x) \right) p(dx) \geq \int_{\Omega} \Phi(r(x)) p(dx) + \int_{\Omega} r(x) q(dx)$$

for any bounded, measurable $r : \Omega \rightarrow \mathbb{R}$. Moreover, equality is achieved when for each $x \in \Omega$,

$$r(x) \in \partial \Phi^* \left(\frac{dq}{dp}(x) \right) \iff \frac{dq}{dp}(x) \in \partial \Phi(r(x));$$

$\partial \Phi$ refers to the subdifferential. Rearranging yields the desired variational form with the proposed optimizer assuming the normalization condition holds. \square

The optimizer for the generalized Gibbs variational formula is generally not identified, necessitating the normalization condition.

Finally, we turn to the functional $\sup_{\epsilon > 0} \Lambda_{\epsilon}$ defined in (14). Unlike in the Laplace case, i.e., $\Phi(r) = e^r - r + 1$, the objective of the primal minimization problem is not transparent. Below, we show that for the standard quadratic loss corresponds to the primal objective of minimizing variance. In particular, we choose $\Phi(r) = r^2 + 1$ to correspond to having chi-squared regularization in the dual problem, though the specific choice of constant does not matter.

Proposition Appendix A.4. *Let $r : \Omega \rightarrow \mathbb{R}$ be bounded, measurable and let $p \in \mathcal{P}(\Omega)$ be a probability measure. Let $\Phi(r) = r^2 + 1$. Then,*

$$\sup_{\epsilon > 0} \Lambda_{\epsilon}(r) = \sqrt{\mathbb{E}_p[r^2] - \mathbb{E}_p[r]^2}.$$

Proof. First, observe that, for each fixed $\nu \in \mathbb{R}$, the map

$$\epsilon \mapsto \epsilon \Phi^{-1} \left(\frac{\nu}{\epsilon} + \mathbb{E}_p \left[\Phi \left(\frac{r - \nu}{\epsilon} \right) \right] \right)$$

monotonically increases as $\epsilon \rightarrow 0$. This is by the monotonicity of Φ , Φ^* , and $\epsilon \mapsto 1/\epsilon$ as well as the non-negativity of ϵ . Thus, we can replace the supremum by a limit as $\epsilon \rightarrow 0$.

Now, we wish to compute

$$\liminf_{\epsilon \rightarrow 0} \inf_{\nu \in \mathbb{R}} \left\{ \epsilon \Phi^{-1} \left(\frac{\nu}{\epsilon} + \mathbb{E}_p \left[\Phi \left(\frac{r - \nu}{\epsilon} \right) \right] \right) \right\}$$

by switching the limit and infimum. For any $\delta > 0$, let $(\nu^\epsilon)_{\epsilon > 0}$ be a collection of δ -minimizers of the inner infimum, that is,

$$\epsilon \Phi^{-1} \left(\frac{\nu^\epsilon}{\epsilon} + \mathbb{E}_p \left[\Phi \left(\frac{r - \nu^\epsilon}{\epsilon} \right) \right] \right) - \delta \leq \inf_{\nu \in \mathbb{R}} \left\{ \epsilon \Phi^{-1} \left(\frac{\nu}{\epsilon} + \mathbb{E}_p \left[\Phi \left(\frac{r - \nu}{\epsilon} \right) \right] \right) \right\}.$$

Moreover, the map

$$\nu \mapsto \epsilon \Phi^{-1} \left(\frac{\nu}{\epsilon} + \mathbb{E}_p \left[\Phi \left(\frac{r - \nu}{\epsilon} \right) \right] \right)$$

is coercive by the superlinearity of Φ and uniformly so in ϵ . Thus, $(\nu^\epsilon)_{\epsilon > 0}$ is precompact and has a subsequential limit point, which we denote by ν^* . Now, we have that

$$\begin{aligned} \liminf_{\epsilon \rightarrow 0} \inf_{\nu \in \mathbb{R}} \left\{ \epsilon \Phi^{-1} \left(\frac{\nu}{\epsilon} + \mathbb{E}_p \left[\Phi \left(\frac{r - \nu}{\epsilon} \right) \right] \right) \right\} &\geq \liminf_{\epsilon \rightarrow 0} \epsilon \Phi^{-1} \left(\frac{\nu^\epsilon}{\epsilon} + \mathbb{E}_p \left[\Phi \left(\frac{r - \nu^\epsilon}{\epsilon} \right) \right] \right) - \delta \\ &= \liminf_{\epsilon \rightarrow 0} \Phi^{-1} (\epsilon \nu^\epsilon + \mathbb{E}_p [\Phi(r - \nu^\epsilon)]) - \delta \\ &= \liminf_{\epsilon \rightarrow 0} \epsilon \Phi^{-1} (\mathbb{E}_p [\Phi(r - \nu^*)]) - \delta \\ &= \Phi^{-1} \left(\inf_{\nu \in \mathbb{R}} \mathbb{E}_p [\Phi(r - \nu)] \right) - \delta. \end{aligned}$$

On the other hand, we have straightforwardly by comparison that

$$\begin{aligned} \liminf_{\epsilon \rightarrow 0} \inf_{\nu \in \mathbb{R}} \left\{ \epsilon \Phi^{-1} \left(\frac{\nu}{\epsilon} + \mathbb{E}_p \left[\Phi \left(\frac{r - \nu}{\epsilon} \right) \right] \right) \right\} &\leq \inf_{\nu \in \mathbb{R}} \lim_{\epsilon \rightarrow 0} \left\{ \epsilon \Phi^{-1} \left(\frac{\nu}{\epsilon} + \mathbb{E}_p \left[\Phi \left(\frac{r - \nu}{\epsilon} \right) \right] \right) \right\} \\ &= \Phi^{-1} \left(\inf_{\nu \in \mathbb{R}} \mathbb{E}_p [\Phi(r - \nu)] \right). \end{aligned}$$

Therefore, sending $\delta \rightarrow 0$ shows that the limit and infimum can be interchanged.

Finally, we solve the variational problem by checking first-order optimality. The problem is now convex, and straightforward computation yields that the optimal ν is achieved by choosing the mean. This concludes the proof. \square

Appendix B. Physics Informed Machine Learning

Appendix B.1. Global weights

Notice that for first-order optimizers such as ADAM, the update direction (i.e., equation (9)) for PINNs (i.e., equation (24)) is given by:

$$p^k = -m_E \nabla_{\theta} \mathcal{L}_E(\theta^k) - m_B \nabla_{\theta} \mathcal{L}_B(\theta^k) - m_D \nabla_{\theta} \mathcal{L}_D(\theta^k), \quad (\text{B.1})$$

where $\nabla_{\theta} \mathcal{L}_E$, $\nabla_{\theta} \mathcal{L}_B$, and $\nabla_{\theta} \mathcal{L}_D$ are the loss gradients which can be represented as high-dimensional vectors defining directions to minimize their respective loss terms. Notice that if the gradient magnitudes are imbalanced, one direction will dominate, which may lead to poor convergence. To address this challenge, we propose modifying the magnitude of the individual directions by scaling their respective global weights. In particular, we fix m_E and update the remaining global weights using the rule:

$$m_B^k = \alpha m_B^{k-1} + (1 - \alpha) \frac{\|\nabla_{\theta} \mathcal{L}_E\|}{\|\nabla_{\theta} \mathcal{L}_B\|}, \quad (\text{B.2})$$

$$m_D^k = \alpha m_D^{k-1} + (1 - \alpha) \frac{\|\nabla_{\theta} \mathcal{L}_E\|}{\|\nabla_{\theta} \mathcal{L}_D\|}, \quad (\text{B.3})$$

where $\alpha \in [0, 1]$ is a stabilization parameter [81]. This formulation computes the iteration-wise average ratio between gradients, enabling normalized scaling, which, on average, allows us to define a balanced update direction \hat{p}^k :

$$\hat{p}^k \approx -m_E \|\nabla_{\theta} \mathcal{L}_E\| \left[\nabla_{\theta} \mathcal{L}_E(\theta^k) - \frac{\nabla_{\theta} \mathcal{L}_B(\theta^k)}{\|\nabla_{\theta} \mathcal{L}_B\|} - \frac{\nabla_{\theta} \mathcal{L}_D(\theta^k)}{\|\nabla_{\theta} \mathcal{L}_D\|} \right]. \quad (\text{B.4})$$

Under this approach, all loss components have balanced magnitudes, allowing each optimization step to minimize all terms effectively.

Algorithm 1: *vRBA* for PINNs

Input: Representation model: \mathcal{M}
 Training points: X_B, X_D, X_E
 Optimizer parameters: *lr* *vRBA* parameters: $\eta, \lambda_{max0}, \lambda_{cap}, \alpha_g, m_E, \gamma_g$
 Number of iterations per stage: N_{stage}
 Total number of training of iterations: N_{train}
 Boolean flags: *adaptive weights, adaptive distribution*
Output: Optimized network parameters θ

- 1: Initialize the network parameters: θ
- 2: Initialize RBA: $\lambda_{\alpha,i}^0 = 0.1\lambda_{max0} \forall \alpha, i$ with $\alpha = \{B, D, E\}$
- 3: Initialize uniform distribution: \bar{q}_α^k with $\alpha = \{B, D, E\}$
- 4: **for** $k < N_{train}$ **do**
- 5: Update maximum RBA upper bound: $\lambda_{max} = \min(\lambda_{max0} + k/N_{stage}, \lambda_{cap})$
- 6: Update decay rate: $\gamma^k = 1 - \eta/\lambda_{max}$
- 7: **for** each $\alpha \in \{B, D, E\}$ **do**
- 8: **if** *adaptive distribution* **then**
- 9: Update the sampling p.m.f: $\bar{q}_\alpha^k \leftarrow (\lambda_\alpha^k)/\sum(\lambda_\alpha^k)$
- 10: **end if**
- 11: Sample *bs* points from X_α : $X_\alpha^k \sim \bar{q}_\alpha^k$
- 12: Compute network prediction: $u_{\alpha,i} \leftarrow \mathcal{M}(\theta, x_{\alpha,i}^k), \forall x_{\alpha,i} \in X_\alpha^k$
- 13: Compute residuals: $r_{\alpha,i}^k$ using $u_{\alpha,i}$ and equations 1, or 2.
- 14: Update tilted distribution: $q_{\alpha,i}^k$ using equation 20 or 21
- 15: Exponential moving average: $\lambda_{\alpha,i}^k \leftarrow \gamma^k \lambda_{\alpha,i}^{k-1} + \eta^* q_{\alpha,i}^k$
- 16: **if** *adaptive weights* **then**
- 17: Compute loss term: $\mathcal{L}_\alpha^k = \langle (\lambda_{\alpha,i}^k r_{\alpha,i}^k)^2 \rangle$
- 18: **else**
- 19: Compute loss term: $\mathcal{L}_\alpha^k = \langle (r_{\alpha,i}^k)^2 \rangle$
- 20: **end if**
- 21: Compute gradient: $\nabla_\theta \mathcal{L}_\alpha^k$
- 22: Compute the average gradient magnitude : $\|\nabla_\theta \bar{\mathcal{L}}_\alpha^k\| = \gamma_g \|\nabla_\theta \bar{\mathcal{L}}_\alpha^{k-1}\| + (1 - \gamma_g) \|\nabla_\theta \mathcal{L}_\alpha^{k-1}\|$
- 23: **end for**
- 24: Update data global weight: $m_D^k = \alpha_g m_D^{k-1} + (1 - \alpha_g) m_E \|\nabla_\theta \bar{\mathcal{L}}_E^k\| / \|\nabla_\theta \bar{\mathcal{L}}_D^k\|$
- 25: Define total update direction: $p^k \leftarrow -m_E \nabla_\theta \mathcal{L}_E^k - m_D^k \nabla_\theta \mathcal{L}_D^k$
- 26: Update parameters: $\theta^{k+1} \leftarrow \theta^k + lr^k p^k$
- 27: **end for**

Appendix C. Operator Learning

Operator learning aims to approximate mappings between infinite-dimensional function spaces, inspired by the universal approximation theorem for nonlinear operators introduced by Chen and Chen [85]. In contrast to traditional supervised learning, which seeks point-wise mappings, operator learning targets functional input–output relationships, such as solution operators of PDEs. Operator learning is a suitable approach for problems where solutions must be inferred across varying initial or boundary conditions, enabling fast inference once

trained. In this study, we consider DeepONet, Fourier Neural Operator (FNO), and Time-Conditioned UNet (TC-UNet) based architectures.

Appendix C.1. DeepONet

DeepONet consists of two networks - a trunk network and a branch network. The trunk network encodes spatial coordinates and learns a basis in the target function space, while the branch network maps the input function, evaluated at a fixed set of sensors, to coefficients that project onto this learned basis. The resulting dot product yields the output function at each spatial location. This design is rooted in the operator approximation theorem and enables expressive and efficient modeling of nonlinear operators. DeepONet and its variants are widely applied in mechanics [86], high-speed flows [87], materials science [88] and multi-phase flows [89].

Appendix C.2. FNO

FNO learn solution operators by leveraging spectral convolutions in the Fourier domain. The input function is first lifted to a high-dimensional latent space through pointwise linear transformations. A Fourier transform is applied to these lifted features, enabling convolutional operations to be performed as multiplications in frequency space. High-frequency modes are typically truncated to enforce smoothness, reduce overfitting, and improve training dynamics. The result is then transformed back to physical space via the inverse Fourier transform and projected to the target dimension. The global receptive field of FNOs makes them particularly effective for modeling long-range dependencies in solutions to PDEs, as demonstrated in applications such as weather forecasts [90], porous media flows [91], and turbulence [92].

Appendix C.3. TC-UNet

Unlike FNOs, TC-UNet [41, 76] operates entirely in physical space using local convolutions. The architecture is based on a UNet, a hierarchical fully convolutional neural network that captures multiscale features through successive downsampling and upsampling. TC-UNet uses time conditioning via feature-wise linear modulation (FiLM) [93], applied at each level of the hierarchy. This allows the model to adaptively modulate intermediate features based on the time coordinate input, enabling accurate modeling of spatiotemporal dynamics. TC-UNet or UNet-based architectures are particularly well-suited for problems characterized by sharp gradients [87] or fine-scale structures [94] and are, in general, more robust to spectral bias [95, 96] compared to other neural operator architectures.

Algorithm 2: *vRBA* for Operator Learning

Input:

- Representation model (Neural Operator): G_θ
- Training data: $\{v_j, u_j\}_{j=1}^{N_{func}}$ (a set of input/output function pairs)
- Spatial points per function: N
- Optimizer parameters: lr
- vRBA* parameters: $\eta, \lambda_{max0}, \lambda_{cap}, \gamma$
- Batch size for functions: b_u
- Number of iterations per stage: N_{stage}
- Frequency of distribution update: N_{update}
- Total number of training iterations: N_{train}

Output: Optimized network parameters θ

- 1: Initialize the network parameters: θ^0
 - 2: Initialize weights: $\Lambda_{i,j}^0 = 0.1\lambda_{max0}$ for $i = 1..N, j = 1..N_{func}$
 - 3: Initialize function sampling p.m.f. uniformly: $\bar{q}_j^0 = 1/N_{func}$ for $j = 1..N_{func}$
 - 4: **for** $k = 0, 1, \dots, N_{train} - 1$ **do**
 - 5: Update maximum RBA upper bound: $\lambda_{max} = \min(\lambda_{cap}, \lambda_{max0} + k/N_{stage})$
 - 6: Update EMA decay rate: $\gamma^k = 1 - \eta/\lambda_{max}$
 - 7: Sample a batch of b_u function indices $\mathcal{J}_k \sim \bar{q}^k$
 - 8: Compute residuals for the batch: $R_{i,j}^k = G_{\theta^k}(v_j)(x_i) - u_j(x_i)$ for $i \in \{1..N\}, j \in \mathcal{J}_k$
 - 9: Update target distribution matrix for the batch: $Q_{i,j}^{k+1}$ using $|R_{i,j}^k|$ (via Eq. 20 or 21)
 - 10: Update weights for the batch via EMA: $\Lambda_{i,j}^{k+1} \leftarrow \gamma^k \Lambda_{i,j}^k + \eta^* Q_{i,j}^{k+1}$ for $j \in \mathcal{J}_k$
 - 11: Compute the weighted loss for the batch: $\mathcal{L}^k = \frac{1}{b_u N} \sum_{j \in \mathcal{J}_k} \sum_{i=1}^N [\Lambda_{i,j}^{k+1} R_{i,j}^k]^2$
 - 12: Compute gradient of the loss: $g^k = \nabla_{\theta} \mathcal{L}^k |_{\theta=\theta^k}$
 - 13: Update parameters: $\theta^{k+1} \leftarrow \theta^k - lr^k g^k$
 - 14: **if** $k \pmod{N_{update}} == 0$ **then**
 - 15: Aggregate importance scores for all functions: $s_j^{k+1} = \sum_{i=1}^N \Lambda_{i,j}^{k+1}$ for $j = 1..N_{func}$
 - 16: Normalize scores to form new p.m.f.: $\bar{q}_j^{k+1} = s_j^{k+1} / \sum_{\ell=1}^{N_{func}} s_{\ell}^{k+1}$
 - 17: **end if**
 - 18: **end for**
-

Appendix D. Implementation Details

Appendix D.1. Physics-Informed Neural Networks

For our Physics-Informed Neural Network (PINN) benchmarks, we detail two separate experimental setups based on the optimization strategy employed.

Appendix D.1.1. First-Order Optimization

For the Allen-Cahn equation solved with a first-order optimizer, the network architecture and hyperparameters were adapted from previous work in [9]. The specific implementation details are summarized in Table D.5. This setup utilizes the Adam optimizer for the entire training duration and applies *vRBA* as an importance weighting scheme.

Hyperparameter	Allen-Cahn
N. of Adam training iterations	3e5
N. of SSBroyden training iterations	0
Number of hidden layers N	6
Hidden layer dimension H	64
Activation function	$\tanh(\cdot)$
Fourier Feature embedding degree [97]	10
Initialization	$U\left(-\sqrt{\frac{3}{I}}, \sqrt{\frac{3}{I}}\right)$
Learning rate lr	1e-3
lr -Decay rate	0.9
lr -Decay step	5000
Total number of points	2.56e4
Batch size	1e4
vRBA Parameters (Weighting)	
γ (EMA memory)	0.999
η (EMA learning rate)	0.01
ϕ (Smoothing)	0.8
Self-Scaling Parameters	
λ_{max0} (Initial max weight)	10
λ_{cap} (Weight cap)	20
γ_g (Gradient EMA memory)	0.99
α_g (Global weight EMA memory)	0.99975
N_{stage} (Iterations per stage)	50000
m_E (Equation loss weight)	1.0

Table D.5: Implementation details for the Allen-Cahn equation using a first-order Adam optimizer. The self-scaling strategy and hyperparameters are based on [9]. Note that for experiments using the quadratic potential ($\Phi(r) = r^2$), no smoothing was applied ($\phi = 1.0$).

Appendix D.1.2. Second-Order Optimization

For the experiments involving a second-order optimizer for both the Allen-Cahn and Burgers' equations, we followed the methodology presented in [16]. The training begins with 5,000 Adam iterations for robust initialization, after which we switch to the SSBroyden optimizer for the remainder of the training. In this setup, vRBA is applied as an importance sampling strategy, where the collocation points are resampled every 100 iterations. The relevant hyperparameters are detailed in Table D.6.

Hyperparameter	Allen-Cahn	Burgers
N. of Adam training iterations	5e3	5e3
N. of SSBroyden training iterations	6e4	6e4
Number of hidden layers N	3	3
Hidden layer dimension H	30	30
Activation function	$\tanh(\cdot)$	$\tanh(\cdot)$
Periodicity Encoding	$\sin(\cdot), \cos(\cdot)$	$\sin(\cdot), \cos(\cdot)$
vRBA Parameters (Sampling)		
Resampling Frequency	100 iter.	100 iter.
γ (EMA memory)	0.9	0.9
η (EMA learning rate)	0.1	0.1
ϕ (Smoothing)	0.9	1.0

Table D.6: Implementation details for the Allen-Cahn and Burgers’ equations using a second-order SSBroyden optimizer, following the methodology in [16].

Appendix D.2. Operator Learning

For the operator learning benchmarks, the architectures were chosen based on the specific model and task.

Appendix D.2.1. DeepONet

For the Bubble Growth Dynamics task, we employed a DeepONet architecture. The model consists of a branch network to process the input function and a trunk network to process the spatial/temporal coordinates. The implementation details, including the hybrid vRBA strategy, are summarized in Table D.7.

Category	Hyperparameter	Value
Branch Network	Number of hidden layers	4
	Hidden layer dimension	100
	Activation function	GELU
Trunk Network	Number of hidden layers	4
	Hidden layer dimension	100
	Activation function	GELU
Training Details	Optimizer	Adam
	Total N. of Parameters	101,100
vRBA Parameters (Hybrid Strategy)	Method	Weighting (Spatial Domain) & Sampling (Function Space)
	γ (EMA memory)	0.999
	η (EMA learning rate)	0.01
	ϕ (Smoothing)	0.8

Table D.7: Implementation details for the DeepONet used for the Bubble Growth Dynamics benchmark. The vRBA hyperparameters are consistent with those used in the first-order PINN experiments. Note that for experiments using the quadratic potential ($\Phi(r) = r^2$), no smoothing was applied ($\phi = 1.0$).

Appendix D.2.2. FNO and TC-UNet

For the more complex Fourier Neural Operator (FNO) and Time-Conditioned U-Net (TC-UNet) models, we adopted the specific architectures and code provided in the reference TC-UNet study [41]. This approach ensures our results are directly comparable to established benchmarks for these models. Consistent with the DeepONet experiment, we applied the same hybrid vRBA strategy: importance weighting was used for the spatial domain, while importance sampling was applied to the function space.

Appendix D.3. JAX Implementation of the SSBroyden Optimizer

This appendix details our custom JAX implementation of the Self-Scaled Broyden (SS-Broyden) optimizer, which was used for all second-order optimization experiments. The original method, proposed by Urbán et al. [16], relies on modified SciPy routines that are CPU-bound and not directly portable to a JAX-native, GPU-accelerated workflow.

Our implementation preserves the core SSBroyden update logic, which dynamically computes scaling (τ_k) and updating (ϕ_k) parameters. However, the line search portion of the algorithm required a complete rewrite. Due to the absence of SciPy’s advanced line search routines in JAX Scipy, we developed a custom three-stage fallback line search mechanism to ensure robust convergence. This procedure creates a cascade of attempts with progressively less strict Wolfe conditions, starting with strict parameters ($c_2 = 0.9$) and relaxing them ($c_2 = 0.8$, then $c_2 = 0.5$) only upon failure. This adaptation was critical for ensuring the optimizer could consistently make progress on the challenging loss landscapes of the problems studied.